Nano Research
2020, 13(6): 1485–1508
ISSN 1998-0124 CN 11-5974/O4
https://doi.org/10.1007/s12274-020-2750-8

Review Article

Recent advances in photodynamic therapy based on emerging two-dimensional layered nanomaterials

Xinqiang Wu[1,§], Xiaofeng Jiang[1,§], Taojian Fan[2,3,4,§], Zhiwei Zheng[1], Zhaoyuan Liu[1], Yubin Chen[1], Liangqi Cao[1], Zhongjian Xie[2,3,4], Dawei Zhang[1], Jiaqi Zhao[2,3,4], Qiwen Wang[1], Zhenhui Huang[1], Zhijian Chen[1], Ping Xue[1] (✉), and Han Zhang[2,3,4] (✉)

[1] *Department of Hepatobiliary Surgery, the Second Affiliated Hospital of Guangzhou Medical University, Guangzhou 510260, China*
[2] *Key Laboratory of Optoelectronic Devices and Systems of Ministry of Education and Guangdong Province, Collaborative Innovation Centre for Optoelectronic Science & Technology, Institute of Microscale Optoelectronics, Shenzhen University, Shenzhen 518060, China*
[3] *College of Physics and Optoelectronic Engineering, Shenzhen University, Shenzhen 518060, China*
[4] *Shenzhen Key Laboratory of Micro-Nano Photonic Information Technology, Guangdong Laboratory of Artificial Intelligence and Digital Economy (SZ), Shenzhen University, Shenzhen 518060, China*
[§] *Xinqiang Wu, Xiaofeng Jiang, and Taojian Fan contributed equally to this work.*

Received: 23 December 2019 / **Revised:** 5 March 2020 / **Accepted:** 7 March 2020

ABSTRACT

Photodynamic therapy (PDT) is a promising non-invasive therapy approach for various diseases including malignant tumor. The process of PDT involves three interrelated aspects, namely photosensitizer (PS), light source, and oxygen, among which PS is the decisive factor that determines its anticancer efficiency. There exist some defects in currently applied PDT, such as inadequate production of reactive oxygen species (ROS), poor penetration of exciting light, insufficient oxygen supply, and nonselective distribution of PS. With unique physicochemical and optical properties, two-dimensional nanomaterials (2DNMs) have aroused great interest in biomedical fields. 2DNMs-based PDT is promising to significantly improve antitumor efficacy compared to conventional PDT. In this review, we will firstly introduce the underlying mechanism of PDT and how 2DNMs are absorbed and distribute inside tumor cells. After that, we will not only illustrate how 2DNMs-based PDT can enhance tumor-killing efficacy and minimize side-effects through conquering the above-mentioned defects of conventional PDT and the preparation process of 2DNMs, but also elaborate recent advances about 2DNMs-based PDT. Lastly, we will summarize the challenges and future prospects of 2DNMs-based PDT.

KEYWORDS

two-dimensional nanomaterials, photodynamic therapy, photosensitizer, reactive oxygen species

1 Introduction

Most tumors have insidious onset, so patients are often diagnosed at the middle or advanced stage of the tumor and cannot obtain radical resection. For instance, the vast majority of patients with cholangiocarcinoma are poor candidates for curative resection. In addition, palliative chemo-radiotherapy is often ineffective for tumor. Consequently, there is an urgency to develop new medical modalities to improve the clinical prognosis for cancer patients. In recent years, photodynamic therapy (PDT) based on PSs has gradually developed as one of the most promising non-invasive methods to combat malignant tumors [1]. Compared with traditional treatment modalities (surgery, chemotherapy and radiotherapy), PDT is intrinsically safe with higher selectivity to tumor and fewer damage to normal tissues.

Although photodynamic therapy has achieved some success in treating various malignant tumors, its efficacy still needs to further improve. Photosensitizer (PS), as an important medium for PDT to produce tumor-killing reactive oxygen species, is the most critical factor for further optimization of the efficacy of PDT. The first generation of PS is the mixture of porphyrin and its derivatives (HpD), among which porphyrin sodium (Photofrin) is most widely used. It was approved by FDA of United States in 1995 for treating various solid tumors. Since then, it has been extensively employed in clinical practice and achieved significant effect. However, a number of shortcomings exist in the first-generation PSs: complex components, high skin photo-toxicity, poor selectivity for tumor tissues, and low yield of singlet oxygen ($^1O_2$). In order to overcome the shortcomings of HpD, the second generation of PS was developed by modifying the porphyrin structure, which was mainly the derivative of porphyrin compounds, such as porphyrin, chlorin, metal phthalocyanine, and polycyclic quinone. To compare with the first-generation PSs, the second-generation PSs possess higher chemical purity, superior tissue selectivity, higher yield of reactive oxygen species (ROS) and less toxic side effects. Nonetheless, poor water solubility and low bioavailability are the main disadvantages of the second-generation PSs, resulting in their obvious limitation in clinical applications. Apart from lack of suitable PSs in clinical practice, there still remain several challenges in PDT. First, the currently used PSs are mainly excited by visible light with poor tissue penetration, as they are unable to be absorbed at the photo-theranostic window (650–900 nm) where the skin is the most transparent. As a

Address correspondence to Han Zhang, hzhang@szu.edu.cn; Ping Xue, gyeyxueping@163.com

consequence, current PDT is restricted to superficial or luminal tumors like skin, esophagus and bile duct cancers. Second, due to the rapid tumor growth and intrinsic O_2-consumption characteristic of PDT, the availability of oxygen is limited within tumor tissue. Third, although the majority of PSs accumulate in tumor region following topical or systemic administration, there are still a certain number of PSs located in normal tissues. The indiscriminate distribution causes inevitable side-effects and decreased efficiency simultaneously. Fortunately, the above-mentioned problems may be gotten over by the emerging two-dimensional nano-materials (2DNMs) with versatile properties.

Owing to the liquid cascade centrifugation, the size of 2DNMs can be easily adjusted to meet clinical needs, such as achieving the enhanced permeability and retention (EPR) effect to improve the therapeutic effect of cancer, rapid renal filtration to avoid long-term toxicity, and cross the blood–brain barrier. In addition, ultrathin 2DNMs possess large specific surface area, high surface reactivity, as well as multiple active sites, which are beneficial to modify targeted groups (polymers, liposomes, antigens or receptor corresponding antibodies and ligands, etc., expressed in tumor tissues) to enhance the targeting ability. Then, with the thickness-dependent bandgap, the absorption spectrum of 2DNMs is controllable, which is meaningful for the application of PSs. More importantly, there are a legion of members in the 2DNMs group, including graphene and graphene oxide (GO), Xenes (e.g., phosphorene, antimonene, bismuthene, tellurene, and selenene), MXene, transition metal sulfides (MnS_2, SnS, etc.) as well as 2D MOF, and different 2DNMs show unique properties. As a representative of 2DNMs, the graphene exhibits a great drug carrying capacity owing to the strong π–π stacking interactions. Phosphorene is also a rising star in the biological field, which possesses excellent biodegradability and extremely high $^1O_2$ quantum yield. In addition, the heavy element Ta in Ta_4C_3 is sensitive to X-rays, which is beneficial for CT imaging. Due to the above advantages, the development of new high-efficiency nano-photosensitive agents based on 2DNMs has become more and more important in the field of photodynamic therapy.

2 Photochemical reactions

Current treatment strategies for malignant tumors, including surgical resection, chemotherapy, and radiotherapy, are often nonspecific or highly invasive, which may result in severe side effects. Photodynamic therapy is a minimally invasive and efficient treatment alternative to the conventional therapeutic modalities for a wide range of tumors. It involves three prime elements: PS, light of specific wavelength and sufficient amount of molecular oxygen. ROS generated from the photochemical reactions between PS and light irradiation are the main source of cytotoxicity to tumor cells. On absorption of appropriate wavelength of light, PS is activated to excited singlet state, then it goes through a process called "intersystem crossing" to form excited triplet state, which may react directly with ambient substrates by electron transfer to form free radicals like superoxide anion radicals (Type I reaction), or reacts with the ambient O_2 by energy transfer to form $^1O_2$ (Type II reaction) (Fig. 1(a)) [2]. Both of the reactions can cause irreversible damage to the cancer cells and a range of vasculature effects, including transient vascular spasm, the formation of thrombi, vascular stasis, and permanent vessel occlusion, without affecting the neighboring normal tissues [2–5]. Both $^1O_2$ and hydroxyl radicals (•OH) tend to react with the surrounding biomolecules in their immediate vicinity, leading to very short diffusion distance (< 100 nm) [6].

Wang [7] demonstrated that the ultrathin BPNSs were efficient photo-sensitizer as their quantum yield of $^1O_2$ reached as high as 0.91, which is higher than most of the current used PDT agents, by energy transfer from BP to the triplet ground-state oxygen ($^1O_3$). The tremendous enhancement of $^1O_2$ yield was owing to their rich active sites and low electron-hole recombination rate. What's more, high charge-carried mobility also benefits the enhancement of $^1O_2$ production. Moreover, the ultrathin thickness of 2DNMs also endowed them with rapid respond to exoteric light, which was also critical in PDT. As for tellurium (Te) nanodots (Te-NDs), electrons can be motivated from valence band to conduction band upon near-infrared (NIR) illumination, producing plentiful ROS via electron transfer and distinguished photo-thermal effect through non-radioactive relaxation. Results in Lin's experiment showed the valence potential of Te@GSH was greater than the reduction potential of $^1O_2/O_2$, while the energy level of the conduction band value of Te@GSH was higher than the normal redox potential of $O_2/•O_{2-}$, demonstrating that Te@GSH could produce $^1O_2$ through type-II mechanism [8].

Xie's research team found that BPNS has two distinct photoexcitation processes on account of their sub-band structure, through the analysis of photoluminescence spectra and transient absorption spectra [7]. That is, visible and ultraviolet light can activate BP to produce $^1O_2$ and •OH, respectively (Fig. 1(b)), and either of the ROS produced from different process can effectively kill tumor cells. $^1O_2$ is the dominating ROS produced by BP. It can react with surrounding molecules such as unsaturated lipids, amino acids, which are the basis of cells [1].

The damage induced by ROS to biomolecules may irreversibly kill tumor cells through pathways of necrosis, apoptosis or autophagy. Besides, it may lead to tumor ischemia by vascular

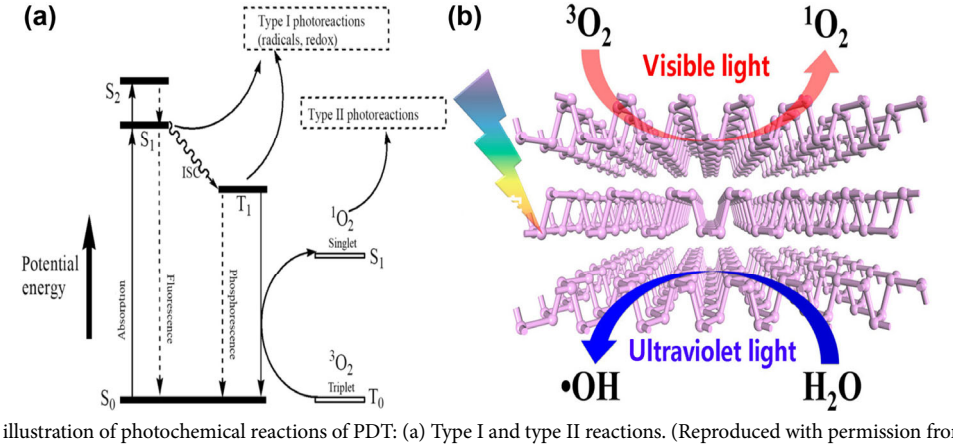

Figure 1 Schematic illustration of photochemical reactions of PDT: (a) Type I and type II reactions. (Reproduced with permission from Ref. [2], © Chinese Pharmaceutical Association and Institute of Materia Medica, Chinese Academy of Medical Sciences 2017). (b) Two distinct photoexcitation processes of BPNSs. (Reproduced with permission from Ref. [7], © American Chemical Society 2018).

injury, and even activate the innate immune response against the cancer [1, 2, 9–11]. Wang et al. [12] fabricated an ultrasmall nanoplatform CS–CD–Ce6 nanoparticles (NPs) that consist of $Cu_{2-x}Se$, β-cyclodextrin, and chlorin e6 (Ce6). The CS–CD–Ce6 NPs could degrade the H_2O_2 within the cancer cells to produce a mass of $^1O_2$ and •OH upon 808 nm laser irradiation. *In vitro* and *in vivo* experiments revealed that the generated ROS could not only directly kill the primary cancer cells, but also evoke immunogenic cell death (ICD) through inducing the immunogenic signals of damage-associated molecular patterns (DAMPs), including calreticulin (CRT), adenosine triphosphate (ATP), and high-mobility group box 1 (HMGB 1). Meanwhile, the CS–CD–Ce6 NPs could induce proinflammatory M1-macrophages polarization which was conducive to tumor suppression as well. Consequently, the as-obtained NPs displayed great efficiency in inhibiting the growth of primary tumor and the recurrence and metastasis upon laser irradiation. In a most recent report, Jin et al. [13] designed a multifunctional hydrogel employing 2D MoS_2 NSs, PC10A and doxorubicin (DOX) through a layer-by-layer approach. Experiments showed a remarkable antitumor efficiency through the combination of chemotherapy, photothermal and photodynamic therapy. Besides, *in vivo* experiment demonstrated that the PC10A/DOX/MoS_2 hydrogel could also elicit anticancer immune response under laser irradiation, so the remote lung metastatic lesions were well controlled simultaneously.

3 Cellular uptake and subcellular localization

Subcellular localization of PSs determines the therapeutic efficiency of PDT. The subcellular localization is the primary site of photodamage induced by the PSs upon irradiation. The subcellular localization sites of PSs include mitochondria, lysosomes, plasma membrane, endoplasmic reticulum (ER) and the nucleus. Tsubone et al. demonstrated that a similar photodamage to lysosome could inhibit proliferation of tumor cells more effectively than to mitochondria [14]. To evaluate the influence of cellular internalization on PDT efficiency, Van Lith et al. constructed two different PSs with or without cell-penetrating peptides (CPPs), which can mediate the cellular uptake of biomolecules, and compared their antitumor effects [15]. Results showed that the PS without CPPs was significantly more effective in inducing cell death than the PS conjugating CPPs, demonstrating that the association with cell membrane is of vital importance for improving the efficiency of PDT. Martins et al. tested their hypothesis that the dysfunction of autophagy caused by PDT might lead to cell death effectively [16]. They finally uncovered a novel paradigm that parallel photodamage to mitochondria and lysosomes could simultaneously activate and inhibit autophagy, resulting in cell death efficiently. Therefore, accurate understanding of cellular uptake and subcellular localization of PS is conducive to developing organelle-target PS with higher antitumor efficacy.

Huang et. al [17] studied the cellular uptake of GO through monitoring the Raman signals inside the cells by using the surface-enhanced raman spectroscopy (SERS) combined with transmission electron microscopy (TEM) and fluorescence microscopy, and revealed the inhomogeneous distribution of the Au-GO inside the cells and found that the internalization of Au-GO was mainly through endocytosis, which was energy-dependent and was mediated by clathrin (Fig. 2(a)). To explore the subcellular localization of BP, Zhao' team [18] developed a totally new Raman active substrate to detect the cellular uptake behavior of BP-based nanocomposites through SERS. They finally demonstrated that the nanocomposites were mainly internalized via caveolae-dependent endocytosis and macropinocytosis, which are energy-dependent, followed by transportation to the lysosome and ER (Figs. 2(b) and 2(c)). The intracellular behaviors of BP are quite different from another 2DNM MoS_2 NSs [19], which were internalized through three different processes: micropinocytosis to late endosomes and then lysosomes, caveolae to early endosomes and then lysosomes, and clathrin to early endosomes and then lysosomes. Yang [20] used various pathway inhibitors and confocal laser scanning microscopy to inspect the endocytic pathway of Te-NDs and found that Te-NDs were mainly internalized by cells via endocytosis that was mediated by clathrin. Further observing revealed the lysosomal disruption upon irradiation after Te-NDs

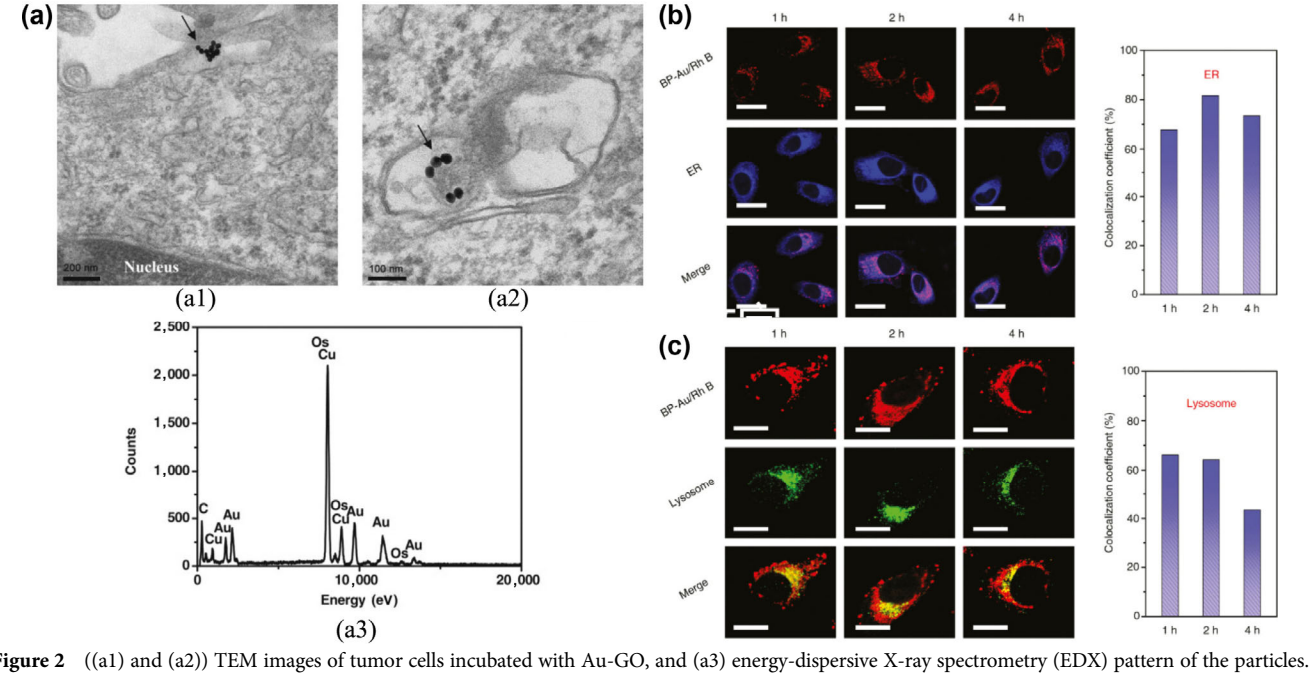

Figure 2 ((a1) and (a2)) TEM images of tumor cells incubated with Au-GO, and (a3) energy-dispersive X-ray spectrometry (EDX) pattern of the particles. (Reproduced with permission from Ref. [17], © WILEY-VCH Verlag GmbH & Co. KGaA, Weinheim 2012). Fluorescence co-localization analysis and colocalization coefficients of BP-Au NSs with (b) ER and (c) lysosome at different time points. (Reproduced with permission from Ref. [18], © Zhiming Liu and Zhouyi Guo et al. 2018).

were endocytosed into lysosomes, which was caused by intracellular ROS. Experimental evidences have demonstrated that the cellular uptake of 2DNMs favors the pathway of endocytosis that was mediated by receptor. Mao [21] presented the process of endocytosis of graphene based on coarse-grained (CG) simulations and theoretical derivation. CG simulations showed that there was a process of flat vesiculation during the receptor-mediated transport of 2DNM. They also revealed the revolution and self-rotation of the 2DNM during membrane wrapping. The mechanism can be extended to all 2DNMs as the above model and approach were universal. Tao [22] showed us the interactions between antimonene-PEG NSs with biology at cellular level. Results revealed that the cellular uptake of antimonene-PEG NSs was via macropinocytosis and caveolin-dependent endocytosis pathways, which was energy-dependent, then transported through "early endosomes" to "late endosomes" and then to "lysosomes" via the endocytosis process.

4 Exciting light source

In order to bring the photodynamic potentiality of 2DNMs into its full play, the exciting illumination must be of appropriate wavelength to penetrate the target deep-inside tissue and meanwhile energetic to generate $^1O_2$. With the great developments of photonic technologies, lasers have been conventionally used as PDT light source because they can emit intense light of specific wavelength with adequate power for effective PDT activation [23]. The light emitting diodes (LEDs) are alternative to lasers which can emit a light of a specified wavelength and provide a homogeneous light distribution for target cells [24].

BP is a metal-free layered semiconductor with wide range band gaps (0.3–2.0 eV) that can respond to a wide range of wavelengths of ultraviolet–visible region of light. Researchers have demonstrated that BP can be efficient PS for the production of $^1O_2$ upon visible light [25, 26]. In addition, Wang's group found that BP NSs can not only produce $^1O_2$ upon visible light illumination but can also generate •OH under ultraviolet excitation owing to their sub-band structure [7].

However, visible and ultraviolet light cannot pass through thick tissues because of light scattering and absorption, which may limit further biomedical applications of BP. NIR light penetrates tissues deeper than ultraviolet and visible light as their absorbance for bio-molecules is minimal in optical window (700–1,000 nm) [27–30]. Therefore, NIR light has deeper penetration across the biotissue that can be as long as 1.5 cm. Moreover, NIR light causes little damage to surrounding normal tissues as lipids and hemoglobin absorb much less NIR light than ultraviolet and visible light. Nonetheless, many 2DNMs cannot efficiently produce $^1O_2$ under direct NIR light illumination. Thus, converting low-energy but deeply penetrating NIR light to high-energy visible light or ultraviolet light to cure deep-seated tumors without sacrificing its efficacy for $^1O_2$ production is necessary [27, 31]. One strategy developed very recently to address this issue is the combination of PS with up-conversion nanoparticles (UCNP) that can be excited by NIR light for deeper penetration. Under low-energy NIR light excitation, UCNP is capable of emitting high-energy ultraviolet or visible light that can induce the PS to generate $^1O_2$ for killing tumor cells. With ability of deeper penetration of NIR light, UCNPs that can be activated by NIR light was able to activate PS in deep-inside tumor tissues, compared to the conventional ultraviolet and visible light induced PDT [32, 33]. Lv's group presented a new UCNP–BPNSs composite with enhanced anticancer properties [34]. In order to obtain the higher UC emission for more efficient PDT, a core–shell $NaGdF_4$:Yb,Er@Yb@Nd@Yb structure was designed, and the results indicated that the process of fluorescence resonance energy transfer facilitated the energy transfer from UCNPs to BPNSs efficiently. Under 808 nm NIR light illumination, the nanocomposite exhibited a great ROS production ability, leading to excellent antitumor properties *in vitro* and *in vivo*. Dibaba [30] developed a novel nanocomposite UCNP–BPNS, in which BPNS was synthesized by liquid exfoliation and NaYF4:Yb,Er@NaGdF4 core–shell (UCNP) was synthesized by solvo-thermal process. Upon 980 nm NIR laser illumination, UCNP converted the energy of light into luminescence with high energy and transferred partial energy to BPNS via FRET, by which way large amounts of $^1O_2$ is generated and about 71% cancer cells were killed by PDT. What's more, when irradiated under 808 and 980 nm laser simultaneously, more than 90% cancer cells were killed as a result of the synergetic photothermal and photodynamic effects of the composite.

X-ray is another promising source to overcome the limitation of penetration depth for deep-inside PDT, owing to its tissue penetration ability that is nearly limitless. Consequently, X-ray activated PDT has aroused great interest [35]. Huang's team [36] grew Bi_2O_3 NPs on the surface of BPNSs to form BP/Bi_2O_3 heterojunction and applied the nanomaterial to X-ray induced photodynamic synergistic radiotherapy treatment *in vivo* (Fig. 3). By this means, they realized the efficient generation of $^1O_2$ induced by X-ray activation and promoted the efficacy of killing tumor cells. In addition to above-mentioned PDT-excited methods, internal light excited PDT (ILE-PDT) is also a promising therapy modality for deep-inside tumors. In this process, the PSs are activated by chemical or biological reaction within bio-tissues, which is called chemo-luminescence or bioluminescence. In this way, there's no need to concern about the penetration depth or the damage to the surrounding tissues as the PDT procedure involves no external light. More efforts should be devoted to exploring the application of ILE-PDT based on 2DNMs.

5 Oxygen supply

To ensure lethal toxicity to tumor cells, sufficient $^1O_2$ must be produced during the whole period of illumination. Therefore, a steady stream of supplies of oxygen is indispensable [37, 38]. However, the hypoxia microenvironment in malignant tumors limits the biomedical application of PDT due to the insufficient oxygen supply. What's worse, the damage to the vasculature induced by PDT and the continual consumption of surrounding molecular oxygen by the PSs themselves for generating $^1O_2$ may aggravate tumor hypoxia, leading to lower treatment efficiency of PDT and even resulting in insensitivity for various treatment modalities like radiotherapy and chemotherapy, as well as the following PDT itself [39, 40]. Hypoxia may be one of the main mechanisms that promote tumor formation in tumor microenvironment [41]. What's more, hypoxia can give rise to the accumulation of hydrogen peroxide, which may activate hypoxia-inducible factor-1α (HIF-1α) associated signaling pathways, and vascular endothelial growth factor (VEGF), both of which can increase the tumor metastatic efficiency and induce resistance to treatment. Therefore, it is necessary to develop strategies for supplying oxygen to the tumor to alleviate hypoxia and realize the highly efficient photodynamic potential of 2DNMs.

To overcome tumor hypoxia, many efforts have been devoted to supply molecular oxygen into the tumor regions, such as hyperoxygenation through the inhalation of pure oxygen by patients at high pressure during PDT, tumor vasculature

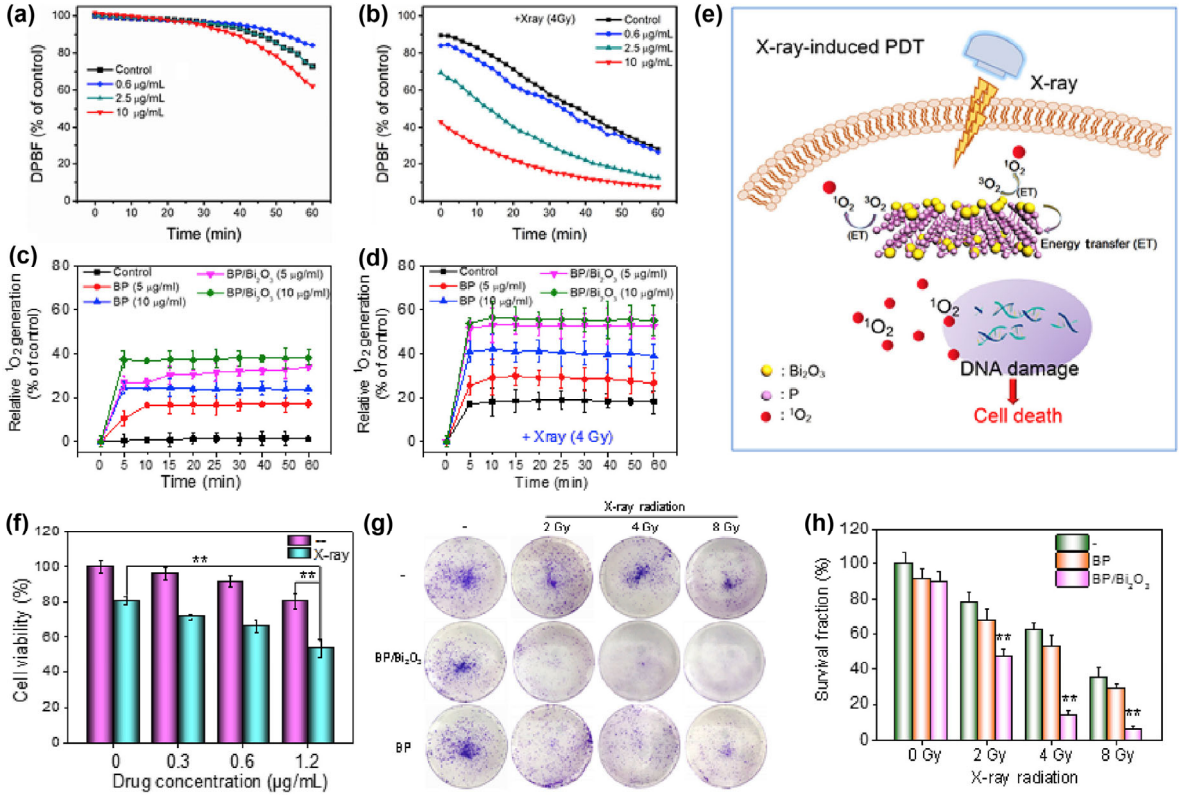

Figure 3 X-ray-PDT performances: (a)–(d) singlet oxygen production by BP/Bi_2O_3 NSs without and with X-ray radiation. (e) Schematic illustration of BP/Bi_2O_3 NSs sensitized X-ray-PDT. (f)–(h) Antitumor performances of BP/Bi_2O_3 based X-ray-PDT for A375 cells. (Reproduced with permission from Ref. [36], © Elsevier Ltd 2018).

restoration, delivering the hemoglobin, and generating O_2 from H_2O_2, among which self-supply of O_2 from environmental H_2O_2 has been proven as a simple and efficient method. Recently, Liu's group designed and fabricated a dual-triggered oxygen self-supply heme dimer derivatized BPNS nanosystem through catalyzing endogenous hydrogen peroxide to generate oxygen [42]. After that, they developed a novel nanoplatform with peroxidase MnO_2 to catalyze the endogenous H_2O_2 in tumor regions to generate oxygen for enhancing photodynamic therapy against hypoxia by taking advantages of BP-based nanocomposite (Fig. 4(a)) [39]. Ma [43] and co-workers developed a novel method that combined the controllable production of O_2 and mitochondrion-targeting strategy for highly effective PDT. The strategy was based on the two-dimensional C_3N_4-Fe NF (fusiform Fe^{III}-doped C_3N_4 nanomaterials), in which the Fe^{III} served as a peroxidase-like catalyst that exhibited a superb catalytic property for converting H_2O_2 in the tumor cells to oxygen and thus relieved the hypoxic condition and improved the PDT efficiency (Fig. 4(b)). What's more, the doping of Fe^{III} enables the PS with magnetic resonance imaging (MRI) contrast ability for simultaneous imaging. Ouyang [44] used BPNSs to fabricate 2D Pt@BP nanocomposites, which integrated the photodynamic potential of BPNSs and the catalytic activity of Pt NPs, through a simple *in situ* growth method. BPNSs served as a PS for yielding $^1O_2$ and a stabilizer at the same time. Pt NPs endowed Pt@BP nanocomposites with catalytic activity, which transferred H_2O_2 into O_2 and thereby efficiently elevate the O_2 amount to alleviate the tumor hypoxic condition and further improve $^1O_2$ production ability of BPNSs (Fig. 4(c)). Besides, Pt@BP nanocomposites could lower the expression level of apoptotic resistance-related factors like HIF-1α, which lightened the resistance to the treatment. Lan's group fabricated a BPQDs/Pt-hybridized mesoporous silica framework decorated with aptamer TLS11a (Apt-BMSF@Pt), in which BMSF@Pt could provide oxygen at H_2O_2 condition (Fig. 4(d)), and TLS11a aptamer could enable the Apt-BMSF@Pt active targeting to HCC. By this way, the enhanced efficiency of antitumor was achieved during the PDT process [45].

However, some researchers concerned that the concentration of H_2O_2 inside tumor cells was not so high as to be used to supply enough oxygen for PDT. Inspired by green plants that could produce oxygen through light and water, *in situ* photocatalytic water-splitting might be an efficient approach to generate sufficient oxygen for overcoming the hypoxic problem of tumors as there are plenty of water within biological tissues. Jiang et al. proposed a novel strategy that could not only generate abundant oxygen but also increase blood perfusion, so as to relieve the hypoxia of tumors for efficient PDT [46]. They obtained ultrathin graphdiyne oxide (GDYO) NSs from graphdiyne to supply oxygen through water splitting and generate $^1O_2$ (Fig. 4(f)), and modified with iRGD-decorated red blood membrane for targeting. Besides, GDYO NSs could also convert light to heat as a photothermal agent that improved blood flow. The fabricated material finally proved to be a brilliant antitumor nanoplaform upon near infrared irradiation. Apart from offering oxygen, type I PDT without consuming oxygen is another way to overcome the hypoxic problem. Zhang et al. synthesized ultrasmall Bi_2WO_6 NPs (~ 5 nm) modified with carboxylic acid groups that was soluble and stable in water [47]. The obtained Bi_2WO_6 NPs could efficiently oxidize H_2O to •OH under 808 nm laser irradiation without consuming molecular oxygen. What's more, the contained metal atoms W and Bi endowed Bi_2WO_6 NPs with great CT imaging capability. Meanwhile, the Bi_2WO_6 NPs possessed the excellent ability of transforming light to heat for photothermal therapy (PTT). The Bi_2WO_6 NPs were demonstrated to be a prominent multifunctional nanoplatform for suppressing malignant cancer in an oxygen-free manner.

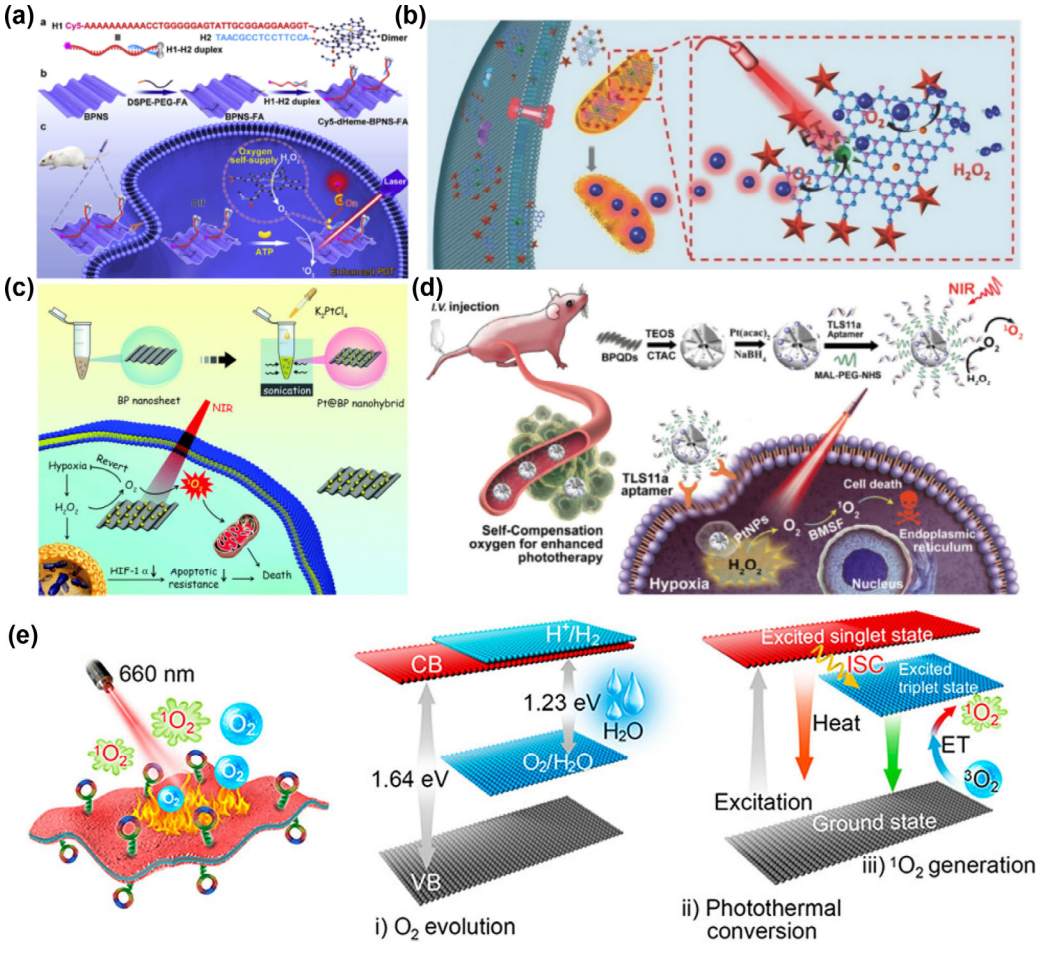

Figure 4 (a)–(d) Schematic illustration of O_2-supporting mechanism of nanosystems through catalyzing H_2O_2 to produce O_2: heme dimer-BP nanosystem (Reproduced with permission from Ref. [39], © Elsevier Ltd 2018) (a), C_3N_4-Fe NF (Reproduced with permission from Ref. [43], © WILEY-VCH Verlag GmbH & Co. KGaA, Weinheim 2016) (b), Pt@BP nano composites (Reproduced with permission from Ref. [44], © The Royal Society of Chemistry 2018) (c), BMSF@Pt nanoplatform (d). (e) Schematic illustration of splitting water to generate O_2 and generate $^1O_2$. (Reproduced with permission from Ref. [45], © American Chemical Society 2019).

6 Ambient stability

Ultrathin 2D nanomaterials, which include quantum dots (QDs), NPs, and NSs, have aroused enormous interest in biomedical applications, owing to their unique physical structure and excellent optical properties. However, an overriding challenge limiting the practical use of 2DNMs is their vulnerability to the ambient condition. For example, within the puckered honeycomb structure of BP, every phosphorus atom covalently binds with the neighboring phosphorus atoms, leaving one pair of electrons exposed outside. The lone pair electrons, as an excellent active site of $^1O_2$, is readily to interact with ambient oxygen to form P_xO_y, leading to the degradation of BP [48]. For BP, the fewer layers, the worse stability [49]. Although the underlying mechanism of its degradation still remains indistinct, studies have shown that BP is unsteady in the presence of oxygen, ROS [50], water, and light [51]. The experiments from Favron [52] revealed a thickness-dependent photo-activated oxidation of BP by aqueous oxygen and that the oxidation rate depends on concentration of oxygen and light intensity linearly and exponentially on the square of energy gap. In order to exert the photocatalytic performance of 2DNMs, it is of vital importance to enhance the ambient stability of 2DNMs. Up to now, strategies used to stabilize 2DNMs relied on isolating its surface from ambient condition to prevent the lone pair electrons exposing to the degradation factors like oxygen and water. Besides, chemical passivation is also commonly utilized to ensure the optical and electronic properties of 2DNMs.

Physical encapsulation is the predominant strategy to enhance the stability of 2DNMs through isolating it from ambient condition with various kinds of materials. Qiu [53] functionalized BPNS with PEG-NH_2 through electrostatic absorption to enhance the physiological stability and biocompatibility. Results showed that the BPNS exhibited improved stability in phosphate buffered solution (PBS) after PEGylation. Liu encapsulated the BPQDs into styrene-acrylamide copolymer nanospheres to achieve better stability [54]. Tao [22] introduced DSPE-PEG to modify the antimonene NSs through hydrophobic interactions and van-der-Waals forces, which could facilitate their stability. Chen [55] modified the thin BPNS with PEG and polyethylenimine (PEI) (Fig. 5(a)). The average thickness of the obtained NS was only 3 to 4 nm (Fig. 5(b)). After 72 h in PBS solution with pH 7.4 (Fig. 5(c)), or in PBS with pH 5.0 (Fig. 5(d)), atomic force microscopy (AFM) images revealed a little decrease of average size in the acidic environment, indicating the improved physiological stability after modification. Liu [56] prepared MoS_2 NSs by lithium intercalation with modification of lipoic acid-terminated PEG (LA-PEG) to obtain PEGylated MoS_2 NSs (MoS_2-PEG), and revealed that PEGylation could greatly improve the stability of MoS_2 NSs in physiological solutions than naked MoS_2 (Fig. 5(e)) while still retaining the high absorbance in NIR region (Fig. 5(f)). Gao [57] coated BPNS with polydopamine (PDA) to construct a stable nanomaterial BP@PDA-PEG-FA, in which polymer mercapto group-poly (ethylene glycol)-folic

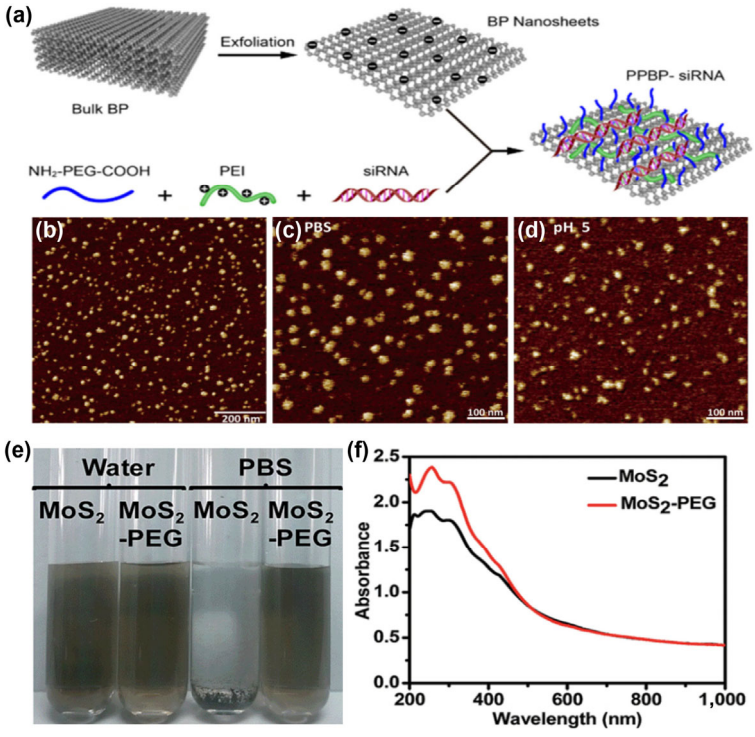

Figure 5 (a) Schematic illustration of the preparation process of BPNS-based nanoplatform. (b) AFM image of the BPNS-based nanoplatform. (c)–(d) AFM images of the BPNS-based nanoplatform in PBS (pH 7.4) and PBS (pH 5.0) after 72 h. (Reproduced with permission from Ref. [55], © American Chemical Society 2018). (e) Picture of MoS_2 NSs and MoS_2-PEG in pure water and PBS (pH 7.4). (f) Light absorption spectra of MoS_2 NSs and MoS_2-PEG. (Reproduced with permission from Ref. [56], © The Royal Society of Chemistry 2014).

acid (HS-PEG-FA) was modified for targeting. Furthermore, the nanomaterial was loaded with chemotherapeutic Dox. Both *in vitro* and *in vivo* experiments demonstrated that the BP-based nanomaterial exhibited improved stability with excellent synergistic anticancer effect. Liu prepared a highly stable TiO_2-NSs@BP nanocomposite through liquid exfoliation assisted by sonication under a hydro-oxygen environment [58]. Results showed that after three cycles of ultraviolet to visible light irradiation, the photo-degradation rate of the nanocomposite still remained 92.5%, revealing stable photocatalytic cycling performance. Furthermore, the TiO_2-NSs@BP nanocomposite displayed higher cycling stability under a hydro-oxygen environment, as the TiO_2 NSs may act as an effective protective layer.

Chemical passivation is also a commonly used strategy to keep 2DNMs stable. Lin [8] decorated Te-NSs with glutathione (GSH) and the results showed that the color of Te@GSH solution remained the same after seven days, while the color of the Te-NSs solution turned obviously, revealing that GSH could keep Te-NSs from oxidation. In other words, GSH decoration could greatly ameliorate the stability of the Te-NSs in aqueous solution. Zhang et al. [59] synthesized graphene-BP hybrid by one pot chemical vapor transport method to enhance the photocatalytic activity and stability of BP. The peak of P–O bond barely increased after exposure in air for about 2 weeks, indicating a significant enhancement of stability. It was the formation of P–C bond in hybrid that resulted in largely decreasing of the oxidation sites in BP. Xing [60] used HfO_2 to passivate BP by depositing HfO_2 on the surface through magnetron sputtering approach, by which way the P atoms in BP were chemically stabilized. With HfO_2 passivation, the mobility remained at 100 to 200 $cm^2/(V{\cdot}s)$, and the current on/off ratio keeps ~ 10^3 after exposure for several weeks. Besides, its electron transfer characteristic can keep steady for about 7 days.

In addition, a number of studies have revealed that doping is another effective method to stabilize and enhance the physicochemical properties of 2DNMs. Yang had presented the Te doping BP with enhanced stability and excellent performance [61]. Recently, they revealed that sulfur doping might be more efficient than Te [62]. Experiments showed that with the exposure time increasing, the mobility and I_{on}/I_{off} ratio of the undoped BP dropped rapidly, while the decrease of mobility was very slow and the I_{on}/I_{off} ratio remained as high as ~ 10^3 for the S-doped BP. Besides, the small and evenly distributed bubbles, and the slower damping of thickness further confirmed the intensive steadiness of S-doped BP. Other methods have also been employed to improve the steadiness of 2DNMs like heterostructure, antioxidant molecules and so on [50, 63, 64].

7 Targeting

There are three critical features for a successful photodynamic action [37]. The exciting light source must be of an appropriate wavelength to be absorbed with enough penetration depth, the oxygen supply must be present in sufficient quantities so as to induce lethal effect to the cancer cells, and the PS must be mostly accumulated within target tissues or cells so that the photo-damage induced upon irradiation would be confined within the sensitive region without implicating the normal tissues. When administered intravenously, the clinically used conventional PSs will distribute indiscriminately throughout the body through blood circulation, not only at the tumor regions but also normal organs and tissues. Although not much damage is induced even at high PS concentrations in healthy organs due to the absence of excitation light to them, patients still need to avoid direct light illumination from the sun and daylight lamps for a considerable period of time, sometimes for several months, before and after implementing the PDT process. Therefore, we need to design cancer-selective PSs to enhance antitumor efficiency and simultaneously avoid undesirable systemic side effects. On the one hand, 2D nanomaterials of

appropriate size are prone to be preferentially up-taken or be detained by malignancies mainly due to the poor vascularization in these tissues, which is called EPR effect [65]. On the other hand, a number of groups have been employed to enhance the targeting ability of 2D nanomaterials.

A targeting molecule, which exhibits a high affinity for specific molecule that is overexpressed on cancer cells, is employed to embellish nanomaterials to enhance the accumulation in cancer cells and simultaneously minimize the adverse effects to normal cells [66]. RGD (Arg-Gly-Asp) peptide has been utilized to conjugate with nanomaterials for cancer therapy, which tends to bind with cell membranes through αvβ3 integrins. Introduction of the targeting RGD to BP nanomaterial can result in the RGD/integrin-mediated cancer-targeting ability and induces precise damage to the cancer cells (Fig. 6(a)) [67]. Wan [68] elaborately fabricated a novel multifunctional nanocarrier based on 2D C_3N_4 NSs (NS-C_3N_4) with dual targeting ability through combining the peptide- and magnetism-mediated targeting (Fig. 6(b)). Results of flow cytometry showed more cellular uptake of the NS-C_3N_4 based nanocarrier than that of control group without RGD by a great deal, indicating the existence of peptide-mediated targeting. In another experiment, an increased ingestion of the NS-C_3N_4 based nanocarrier with a magnet applied was clearly observed, implying the magnetism-mediated targeting. *In vitro* studies had demonstrated the efficient dual targeting greatly enhanced the antitumor efficiency of the NS-C_3N_4 based nanocarrier, as the cell viability of two different cancer cells were lower to 16.37% and 18.85%, respectively. To develop the advantage of 1-pyrenylbutyric acid-modified BPNSs (p-BPNSs), NH_2-PEG-RGD was employed as a targeting biomolecule for modification on the surface of p-BPNS to fabricate BP-based nanomaterials (RP-p-BPNSs) with an improved targeting ability for tumors [69]. Assisted by the EDC/NHS couplant, the RGD tripeptides linked with p-BPNSs. *In vitro* and *in vivo* biological experiments showed that RGD modification endow p-BPNSs excellent biocompatibility and precise antitumor ability upon NIR laser irradiation on account of the active-targeting effect between RGD and αvβ3 ligands, which were over expressed on the surface of tumor cells. Folic acid, which could specifically recognize and bind to folate receptor on the cell membrane surfaces that many types of tumors overexpressed, was decorated on the surface of BPQDs via electrostatic interactions to enhance the active targeting capacity of BPQDs [70]. A receptor competition experiment revealed the outstanding tumor targeting effect of FA. With the active tumor targeting effect of FA ligand, BPQDS-PEG-FA/Dox displayed a better antitumor effect than BPQDS-PEG/Dox, leading to more precise accumulation of chemotherapeutic Dox. As expected, *in vivo* experiments indicated the best antitumor effect of BPQDS-PEG-FA/Dox upon NIR laser irradiation. Subcellular organelles play vital roles in cell survival, and subcellular localization of PSs even determines the antitumor efficacy of photodynamic therapy. Among all subcellular organelles, mitochondria are the prominent target of attack for most therapies, because mitochondria are the primary cellular power source that can convert chemicals into adenosine triphosphate (ATP). Wei [71] developed a 2D nano-graphene oxide (NGO) based, cancer cell and mitochondria dual-targeted nanoplatform PPa-NGO-mAb as a novel PS for PDT. The specific cell targeting was due to the interaction between biological ligand and the corresponding receptor (integrin αvβ3 on the membrane of cancer cells and its monoclonal antibody mAb), and the sub-cellular organelle targeting was due to the translocation and the interaction between the polarized NGO and the mitochondria membrane potential (Fig. 6(c)). Besides, results showed that the cytotoxicity of PPa-NGO-mAb could be switched off in an aqueous fluid of the body like blood and the cytoplasm, and switched on in the lipid membrane system like mitochondria membrane, which significantly decreased the photo-damage to normal tissues. A single-stranded DNA aptamer with unique structure, which is thermal stable, lightweight, and immunogenic, has been utilized as a potent biomolecular targeting element for therapeutic targeting purpose. Lan et al. [45] decorated aptamer TLS11a that was hepatocellular

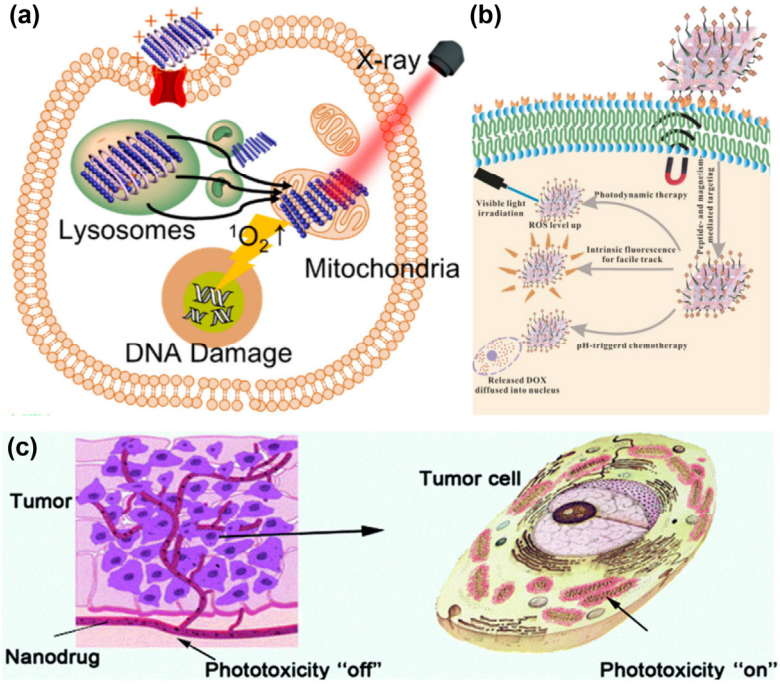

Figure 6 (a) Schematic illustration of the interaction of BP-based nanomaterial with cancer cells. (Reproduced with permission from Ref. [67], © American Chemical Society 2018). (b) Schematic illustration of dual targeting mechanism (peptide- and magnetism-mediated targeting) of 2D C_3N_4 NSs. (Reproduced with permission from Ref. [68], © American Chemical Society 2015). (c) Schematic illustration of phototoxicity switching and tumor cell mitochondria targeting of PPa-NGO-mAb. (Reproduced with permission from Ref. [71], © The Royal Society of Chemistry 2016).

carcinoma (HCC)-targeted to BPQDs-based nanocomposite to construct a targeting catalyst for precise cancer therapy. By decoration of TLS11a aptamer/PEG, the nanocomposite could actively target to HCC and effectively accumulated in the tumors, resulting in the enhancement of PDT efficacy both *in vitro* and *in vivo*. Others used triphenyl phosphonium to target the mitochondria via membrane potential, poly(2-ethyl-2-oxazoline) ligand conjugation, or hyaluronic acid to improve BP-based nanomaterials accumulation at tumor sites and enhance antitumor efficacy.

8 Preparation of 2DNMs

Since the advent of graphene in 2004, the 2DNMs family has developed rapidly, such as graphene group (graphene [72–77], GO [78–81], reduced GO [82–86]), Xenes (phosphine [87–91], antimonene [22, 92–94], borophene [95–100], silicone [101–105], germanene [106–110], stanine [111–114], arsenene [115–120], and bismuthene [121–125]), transition metal dichalcogenides (TMDs, including MoS_2 [88, 126–131], TiS_2 [132–137], TaS_2 [133, 138–140], WS_2 [141–146], $MoSe_2$ [147–151], and WSe_2 [152–155]), organic materials [156], MXenes [157–161], graphitic carbon nitride (g-C_3N_4) [162–166], layered metal oxides [167], and layered double hydroxides (LDHs) [168]. With unique physicochemical properties, 2DNMs have shown attractive prospects in many fields, including optoelectronics [125, 169–171], lase [88, 172–175], catalysis [176–179], energy storage [180–183], biomedicine [184, 185] and more. There are a lot of methods for preparing 2DNMs, including mechanical exfoliation [186–189], liquid phase exfoliation [190–193], chemical vapor deposition [194–198], and wet chemical synthesis [199–201].

However, due to the particularity of the PS's application, only a few methods can satisfy the clinical requirements. First of all, PS is mainly administered by intravenous injection, which determines the 2DNMs with large size can't meet the requirements. However, if the size is too small, the material is easily excreted from the body via the kidney. Actually, drugs for specific diseases usually require an optimal size range, further increasing the difficulty of 2DNMs fabrication. Secondly, due to the blood circulation, it is inevitable for 2DNMs-based PSs to distribute in whole body, so the 2DNMs should show low toxicity in the dark. Finally, the potential of mass production is also a key factor that must be considered for further clinical applications. In view of the above requirement, the most common method of 2DNMs fabrication in the biological field is liquid phase exfoliation [202–204]. The process of preparing 2DNMs by liquid phase exfoliation is mainly divided into three steps: 1. reducing the energy required to break the interlaminar force of the material; 2. providing stress to exfoliate 2DNMs; 3 purification of 2DNMs with appropriate size by centrifugation. For the first step, the most common approach is to choose the suitable solvent, and the surface energy of solvent can match the energy required for the exfoliation. Most of the solvents used initially possess high boiling points, which are difficult to remove and have biological toxicity that is detrimental to the application of PSs [205–207]. In order to improve the biocompatibility of 2DNMs, solvents with better safety were utilized for the exfoliation of 2DNMs. Qiu et al. [54] used low-boiling isopropanol (IPA) as a solvent to fabricate ultrathin BPNSs as a smart drug carrier. Xue et al. [93] found that ethanol can effectively exfoliate bulk antimony into antimonene NSs, which exhibits extremely high miRNA detection sensitivity. It is found that in some cases, water can also be used for the preparation of 2DNMs. In order to ensure the clean surface of 2DNMs, Tao et al. [208] obtained BPNSs with an average size of 120 nm as well as an average thickness of 1–2 nm in deoxygenated water solvent, as shown in Fig. 7(a). In addition to pure solvents, solutions of polymers or surfactants are also a common choose for 2DNMs stripping. In conventional applications, the surface of the 2DNMs prepared in the solutions tends to leave some polymers or surfactants which are difficult to remove and limits the promotion of this strategy. Fortunately, in the biomedical application, suitable polymers attached to the surface of 2DNMs are beneficial sometimes. For example, Wang et al. [209] obtained BPNSs in human serum albumin solutions for drug delivery platforms. The human serum albumin remaining on the surface of BP effectively enhances the biocompatibility, dispersibility in physiological environment, and drug-loading ability of BPNSs. In addition to utilizing the solvent surface energy, the oxidation reaction, which can effectively increase the layer spacing, is also a popular approach for graphene production. During the exfoliation, the graphite is first exposed to the strong oxidizing agents, and a large number of oxygen-containing functional groups are generated on the surface of each layer. Owing to such functional groups, the interlayer spacing of graphite is significantly increased, resulting in an obviously decrease of interlayer force. Then, a large amount of GO can be obtained with simple ultrasonic treatment. After subjected to a suitable reduction reaction, GO is able to be transformed into reduced GO (rGO). The rich oxygen-containing groups on GO and rGO ensure their good dispersibility in aqueous solution as well as enhanced modification ability and drug loading capacity [210, 211]. Although the above method can prepare layered 2DNMs in large quantities, non-layered 2DNMs, in which the layers are connected by strong bonds instead of van der Waals forces, require other methods to open the interlayer spacing.

As a very important 2DNMs group, the preparation of Mxene requires selective etching of its starting materials MAX (where M is an early transition metal, A is a group A element mainly composed of 13 and 14 groups, and X is C and/or N) to obtain loosely packed $M_{n+1}X_n$ layers, as shown in Figs. 7(c)–7(g). With relatively weak bond connection, A is more active than $M_{n+1}X_n$ layers in MAX, which is a prerequisite for the selective etching. In 2011, Naguib et al. [212] successfully etched Al in Ti_3AlC_2 with HF, and obtained MXene with several atomic thicknesses. The yield of MXene fabricated by this method is very high, but the HF used in the experiments is dangerous and affects the biocompatibility of Mxene. To reduce the risk of reaction and improve the biocompatibility, a novel strategy, which synthesize HF *in situ* by acid reaction of fluoride, was developed [213]. After that, in order to meet the demand for small-sized MXene in the biomedical field, Lin et al. [214] extended the etching time from the initial 2 h to 3 days, and successfully obtained the ultra-thin Mxene with an average size of about 150 nm. With a localized surface plasmon resonance (LSPR) effect induced by the unique semimetal property, Ti_3C_2 exhibits amazing NIR absorption (25.2 L/(g·cm) at 808 nm) and high photothermal conversion efficiency (30.6%). Although the preparation process is completely different from graphene and MXene, the oxidation reaction and etching also have excellent performance in the preparation of borophene. Boron, which is a non-layered material, is difficult to fabricate by conventional top-down methods. Fortunately, under high temperature, Ji et al. [215] oxidized the surface of a thick boron sheets to B_2O_3, which can be easily dissolved in water, while the internal boron nanosheets remained stable. After the surface oxidation-etching treatment, the thickness of boron sheets was successfully reduced from ≥ 15 nm to ≤ 5 nm.

For the second step, sonication is commonly used to provide stress for 2DNMs exfoliation. Sonication can be divided into probe sonication and water bath sonication. The former has

a more direct effect on the sample and the energy is more concentrated, while the latter avoids contamination due to the non-direct contact. Actually, although separate probe sonication or water bath sonication can obtain 2DNMs, their combination is able to further increase the yield of 2DNMs. During the exfoliation process, the ultrasound causes the liquid cavitation to create bubbles. After that, along with the rupture of the bubble, the strong stress effectively breaks the connection between the layers of the sample, realizing the exfoliation of 2DNMs. Compared with mechanical cleavage and CVD, sonication tends to produce some defects on the surface of 2DNMs. Fortunately, some works showed that defects on the surface of 2DNMs will enhance the photo-thermal effect of materials, which may have a positive impact on biological applications [216]. The temperature of dispersion may increase significantly during the exfoliation process, so cooling measures, including coil cooling and ice bathing, are necessary. Notably, some 2DNMs, for example BP, are susceptible to oxidation, so it is beneficial to use a parafilm to protect the 2DNMs from contact with oxygen.

After sonication, there are NSs with various sizes dispersed in solution, but only samples with particular size are suitable for PS applications. In order to obtain high concentration dispersion of 2DNMs with specific size, a cascade centrifugation strategy was developed, as shown in Fig. 7(b). Using an iterative centrifugal cascade, Backes et al. [217] successfully obtained a WS_2 dispersion with a single layer content of 75%. After the above three steps, NSs of uniform size can be obtained for biological applications.

9 2DNMs-based PDT

As an emerging and promising noninvasive treatment modality, PDT has been employed for combating a variety of tumors such as hilar cholangiocarcinoma. Efficiency of PDT mainly depends on the PDT agents that can generate subversive ROS upon laser irradiation with a specific wavelength to kill tumor cells. However, the clinically used PSs are often restricted by low $^1O_2$ quantum yields, leading to unsatisfied antitumor efficiency. Due to the particular physical structure and exceptional optical properties, many 2D nanomaterials can rapidly respond to the external light signals and generate a mass of ROS, mainly $^1O_2$, and exhibited much higher antitumor efficiency than the conventional used PSs, demonstrated by *in vitro* and *in vivo* experiments. Furthermore, when cooperate with other splendid properties like ultra-large surface area, or combine with other treatment modalities like chemotherapy, they can show even more enormous potential in inhibiting the tumor growth. Consequently, 2D nanomaterials are coming into play in PDT for various diseases with promising prospects.

9.1 Mono-elemental 2DNMs

As the first 2D nanomaterial to be explored and studied, graphene has been considered a star 2D nanomaterial with an atomically thin, honeycomb lattice. Graphene possesses outstanding electronic, thermal and optical properties, attributing to its unique zero bandgap structure [219–220]. Ge [28] prepared a novel PS based on 2D graphene QDs (GQDs) through an ordinary hydrothermal approach with polythiophenes derivatives. The GQDs possessed a broad absorption spectrum from ultraviolet to visible region as well as a strong deep-red emission. When assessing the $^1O_2$ quantum yield using disodium 9,10-anthracen-dipropionic acid (Na_2-ADPA) as the trapping agent and RB as the reference PDT agent, it was calculated to be 1.3 at different excitation wavelengths of 538, 549 and 562 nm. What's more, the $^1O_2$ quantum yields were maintained at 1.3 at solutions of different pH values of 6 to 8, as shown in Figs. 8(a)–8(c). The high $^1O_2$ quantum yield of 1.3 was considered to stem from a new mechanism termed multistate sensitization (MSS),

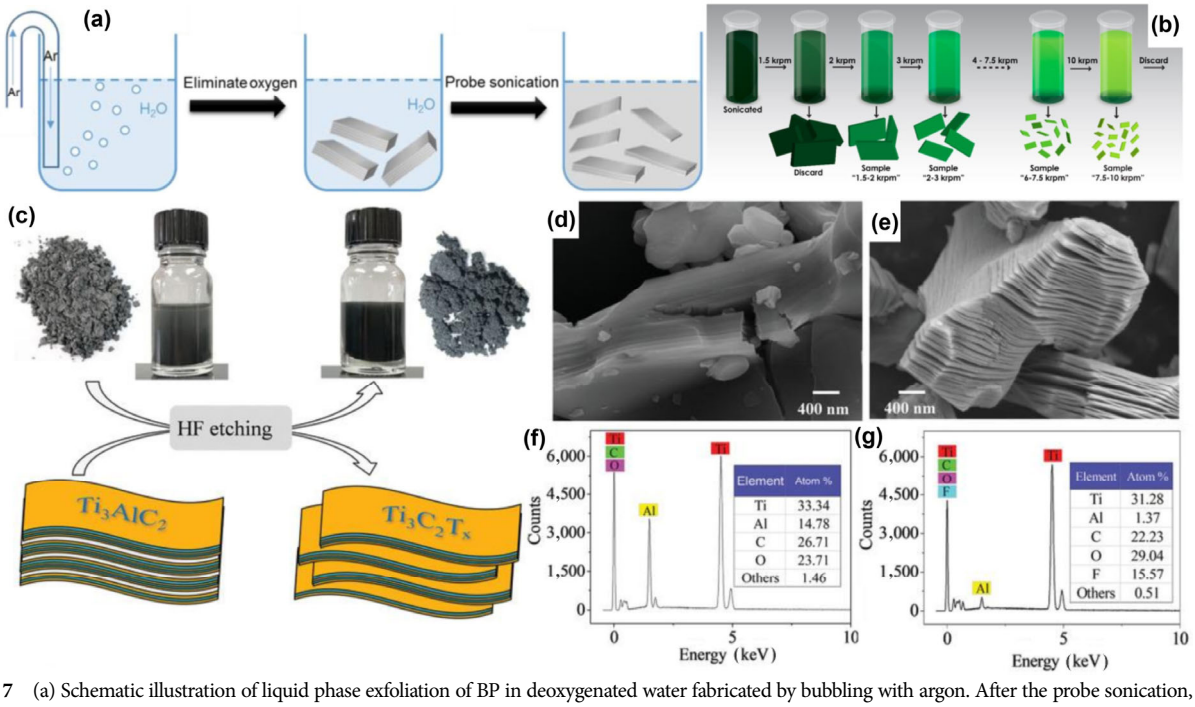

Figure 7 (a) Schematic illustration of liquid phase exfoliation of BP in deoxygenated water fabricated by bubbling with argon. After the probe sonication, BPNSs with various sizes are stably dispersed in water. (Reproduced with permission from Ref. [208], © WILEY-VCH Verlag GmbH & Co. KGaA, Weinheim 2017). (b) Schematic representation of cascaded centrifugation. The first precipitate and the last supernatant should be removed, because the former contains unexfoliated bulk material and the latter contains 2DNMs with extremely small size. The rotational speed of each centrifugal stage is gradually increased to obtain 2DNMs with specific size. (Reproduced with permission from Ref. [217], © American Chemical Society 2015). (c) Schematic illustration of MXene ($Ti_3C_2T_x$) production. (d) and (e) are SEM images of materials before and after etching, respectively. The material etched by HF exhibits a noticeable accordion-like morphology. EDS spectra and elemental percentage of Ti_3AlC_2 (f) and $Ti_3C_2T_x$ (g). (Reproduced with permission from Ref. [218], © WILEY-VCH Verlag GmbH & Co. KGaA, Weinheim 2019).

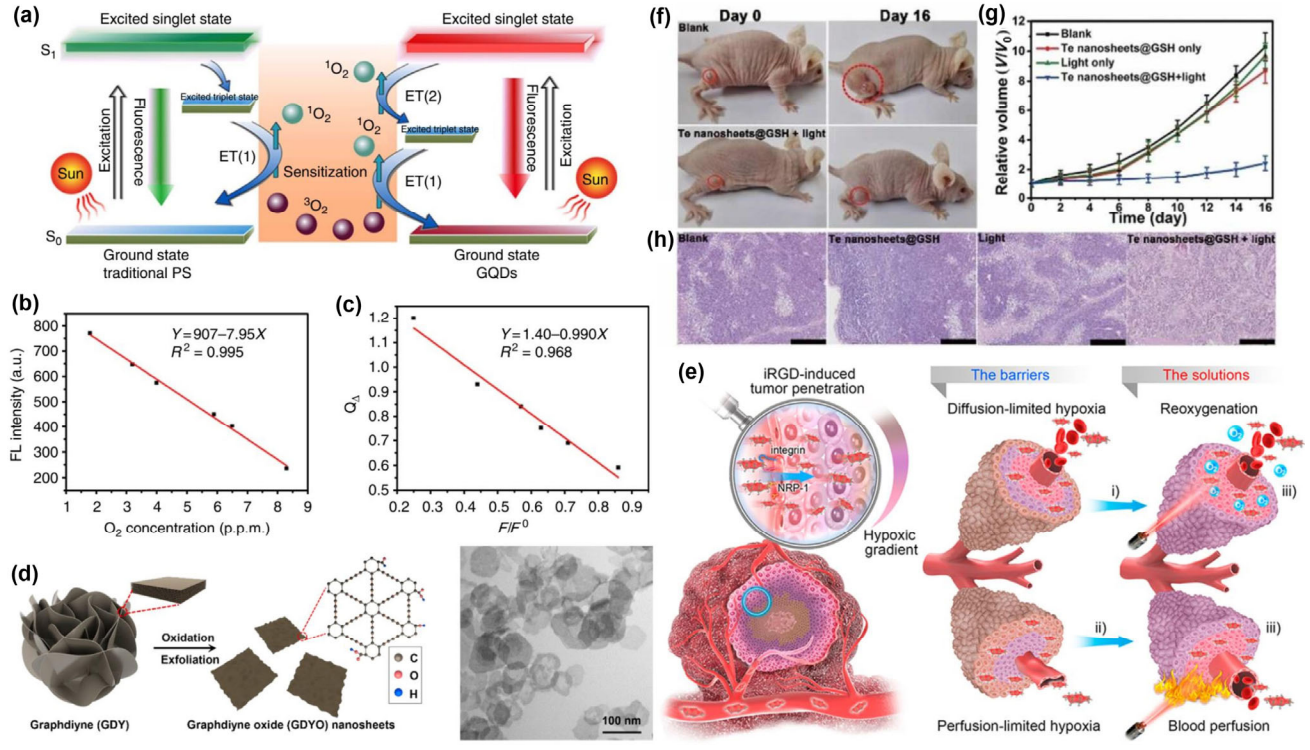

Figure 8 (a)–(c) Graphene-based PDT. (a) Schematic illustration of GQD producing $^1O_2$. (b) Oxygen concentration-dependent fluorescence intensity of GQDs at 680 nm. (c) The dependence of the $^1O_2$ quantum yield on the fluorescence intensity ratio at 680 nm. (Reproduced with permission from Ref. [28], © Springer Nature 2014). ((d) and (e)) Graphdiyne-based PDT. (d) Preparation process and TEM image of graphdiyne. (e) Graphyne-induced O_2 evolution and PTT can overcome O_2-diffusion-limited and perfusion-limited hypoxia barriers. (Reproduced with permission from Ref. [46], © American Chemical Society 2019). (f)–(h) Te-based PDT. (f) Photos of mice before and after treatment. (g) Tumor growth curves of experimental group and control group. (h) H&E stained histological images of tumor sections after different treatments, scale bars are 200 μm. (Reproduced with permission from Ref. [8], © The Royal Society of Chemistry 2018).

which was restricted in the visible region (< 636 nm). In addition to tumor applications, 2DNM-based PDT is also used for in sterilization field to protect endodontically treated teeth from infection. Ghorbanzadeh et al. [221] uses curcumin-loaded GO as a PS to kill enterococcus faecalis, the main microorganism that causes secondary/persistent infection during endodontic treatment. In this work, LEDs, which are suitable for root canal therapy, were used as the light source, and human teeth were selected as the *ex vivo* biofilm model. Compared with the control group, the production of ROS in the experimental group increased by 8 times and showed significant microbial inhibition, indicating a huge clinical potential. As a carbon-based 2DNM different from graphene, graphdiyne also exhibits excellent performance in the field of PDT. Because the valence band maximum below the oxidation potential of water, graphyne has the potential for photocatalytic O_2 evolution, which is beneficial in PDT. The hypoxic environment inside the tumor affects the performance of PDT and promotes tumor metastasis. To solve this problem, Jiang prepared graphdiyne oxide NSs with a size of 120 ± 15 nm and a thickness of ~ 1.7 nm as a novel photosensitizer [46]. The graphdiyne oxide exhibits a band gap of 1.64 eV and effective oxygen generation (the O_2 generation rate can reach ~ 50.3 μmol/(g·h)) as well as long-term stability (30 h) under 660 nm laser irradiation. Further experiments proved that graphdiyne oxide can produce $^1O_2$ to achieve cell killing. Compared with the control group (treated with commercial PS Ce6), graphdiyne-treated cancer cells cultured in the hypoxia box decreased by 84.6%, and the yield of $^1O_2$ increased by 1.78 times. In addition, graphdiyne also has excellent photothermal effect (photothermal conversion efficiency is 60.8%), which can increase blood perfusion and promote oxygen by promoting tumor vasodilation at the tumor site, as shown in Figs. 8(d) and 8(e). Quantitative analysis showed that the average diameter of tumor blood vessels increased from 3.60 to 6.81 μm after graphdiyne-based PDT, and the proportion of tumor hypoxic area decreased from 48.6% to 5.04%. Lin's team [8] fabricated a 2D Te-NSs by a simple liquid exfoliation approach from the corresponding Te raw powder. They found the obtained Te-NSs could be used as PDT agents as the NSs can efficiently generate $^1O_2$ upon light irradiation with 670 wavelength. Experiments showed that the Te-NSs could kill cancer cells or inhibited tumor growth efficiently, as shown in Figs. 8(f)–8(h), indicating their potent photodynamic therapy effects.

9.2 Black phosphorus

As a recently emerged 2DNM, BP nanomaterials have captured great interest because of their outstanding electronic and optical properties [222–225]. As one of the promising photo-catalyst that can produce ROS like $^1O_2$ and •OH under visible or UV light irradiation, BP could be applied for effective photodynamic therapy. BPQDs were first synthesized by Guo's team [26] from natural BP power by solvothermal method in NMP, and its potential as PS was studied. Both *in vitro* and *in vivo* experiments showed that BPQD possessed highly efficient photodynamic effect under 670 nm light irradiation (Figs. 9(a) and 9(b)). BPQD could not only effectively produce reactive oxygen to kill cancer cells, but also had good biocompatibility, and could be quickly cleared outside in a complete form through the renal space. Compared with traditional PSs and other nanostructured PSs, BP has obvious advantages in tumor photodynamic therapy and combination therapy. In 2015, Wang's team first discovered that BP could efficiently generate $^1O_2$, and the quantum yield in saturated oxygen solution could be as high

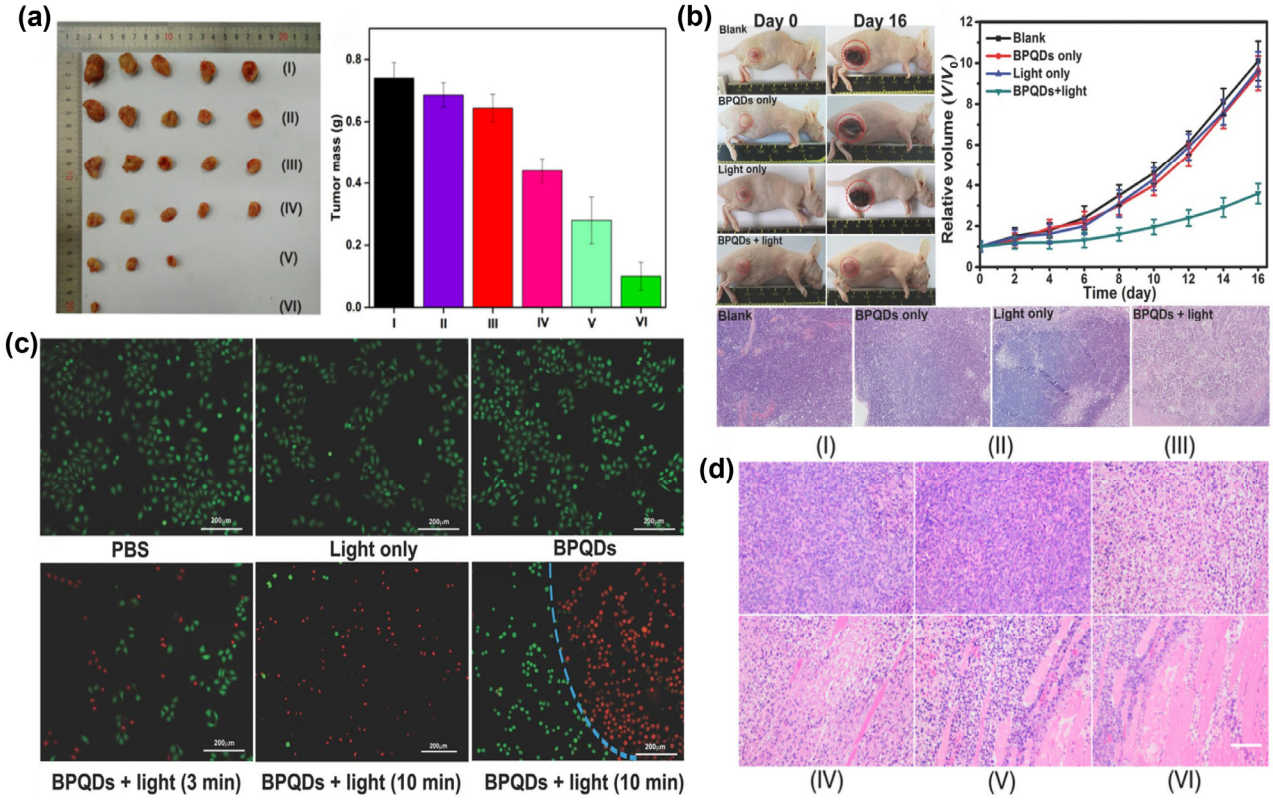

Figure 9 Antitumor performance of BPQDs upon 670 nm illumination: (a) merged inverted fluorescence microscope images of HeLa cells after various treatments (green and red represent live cells and dead cells, respectively). (b) Tumor volume and histological changes after different treatments. (Reproduced with permission from Ref. [26], © WILEY-VCH Verlag GmbH & Co. KGaA, Weinheim 2017). Antitumor performance of BPQDs upon 625 nm and/or 808 nm illumination: (c) tumor volume changes and (d) H&E-stained histological changes (group I, control; II, BPQDs; III, 625 nm light + 808 nm laser; IV, BPQDs + 625 nm light; V, BPQDs + 808 nm laser; VI, BPQDs + 625 nm light + 808 nm laser). (Reproduced with permission from Ref. [227], © The Royal Society of Chemistry 2019).

as 0.91, much higher than that of traditional PSs. Through *in vivo* and *in vitro* experiments, it was found that the application of BP in photodynamic therapy had significant efficacy in treating breast cancer. However, the antitumor campaign may not be easily won by a single therapeutic strategy. Combination of multimodal therapies could be promising to win the battle against cancer. Chen's team [226] presented a novel multifunctional therapeutic system based on BPNSs. The synergistic system not only exhibited much greater drug loading capacity for Dox (950% in weight) than other nano-systems, and pH-/photo-responsive drug release, but potent capacity of efficiently generating $^1O_2$ and photo-thermal activity, thereby displaying dramatically enhanced therapeutic effect for tumor. By controlling hydrolysis-diffusion, Li's team [227] established a BPQDs based multi-functional nano-platform, which could be utilized for tumor biological imaging, PTT and PDT. Combined PDT with PTT has been proved to have synergistic antitumor effect, acquiring a death rate of 96% to the cancer cells (Figs. 9(c) and 9(d)). An appropriate level of hyperthermia induced by PTT may increase tumor cell membrane permeability and thus promote cellular uptake of the PS, as well as improve intra-tumoral blood supply, resulting in increased oxygen supply and thus enhancing $^1O_2$ generation. On the other hand, PDT could enhance the sensitivity of tumor cells to PTT by regulating the microenvironment. As expected, experiments showed that, compared with PTT or PDT alone, this nanomaterial could greatly enhance the tumor killing efficacy. Moreover, its loaded fluorescent molecules could also carry out clear and reliable imaging of tumors. What is noteworthy is that the sequence of therapy modality may influence the antitumor effect. In Chen's study [55], BP nanomaterial irradiated at 808 nm and then at 660 nm exhibited higher antitumor effect than other groups. In contrast, the BP nanomaterial irradiated at 660 nm and then at 808 nm exhibited lower antitumor effect than that in the 808 plus 660 nm group. The potential mechanism may be that the ROS produced by PDT can induce degradation of the BP material and thus hampering the subsequent PTT effect. Yang's team fabricated a new nanocomposite material by loading iron oxide NPs and gold NPs onto few-layer black phosphorus. The material was highly biocompatible, and could effectively inhibit tumor growth through the synergistic effect of NIR laser mediated photo-thermal (gold NPs) and photodynamic (few-layer BP). Moreover, with the MRI visual characteristic of iron oxide NPs, the timing of laser irradiation could be precisely controlled, so as to obtain the best curative effect. Another team [228] developed an imaging-guided and mitochondria-targeting photothermal/photodynamic nanoplatform BP@PDA–Ce6&TPP NSs based on the functionalized BPNSs. In such a nanosystem, polydopamine (PDA) with an excellent photothermal effect was utilized to build a conformal layer on BPNSs, and that could not only significantly enhance the photo-thermal conversion efficiency, provide an amine anchor for further functionalization, but also enhance the stability of BPNSs. Meanwhile a covalently incorporating PS Ce6 with highly efficient ROS production capacity and NIR fluorescence, was employed for PDT and fluorescence imaging, while triphenyl phosphonium (TPP) was used for targeting mitochondria through membrane potential. Experiments revealed that the obtained nanocomposites presented superb synergistic therapeutic effects. Chen et al. [55] designed a biodegradable delivery system based on small and thin BPNSs for human telomerase reverse transcriptase (hTERT) siRNA, which has proven to play a vital role in tumor formation.

Functionalized with positive PEI, the NSs not only exhibited highly efficient in siRNA loading and cellular uptake, but also showed excellent photothermal and photodynamic efficiency upon light irradiation. Experiments showed that the siRNA-loaded BPNSs displayed tremendously enhanced inhibition of tumor growth and metastasis, which was ascribed to the precisely delivery of the hTERT siRNA and the synergistic effect of BP-based PDT and PTT.

9.3 Transition metal dichalcogenides (TMDs)

TMDs are hexagonal lattice composed of two layers of chalcogen atoms and one layer of transition metal atoms. So far, there are about 60 known TMDs, three of which have received significant attention in biological applications: tungsten disulfide (WS_2), molybdenum disulfide (MoS_2), and titanium disulfide (TiS_2). With unique catalytic and optical properties, TMDs have been extensively chemically modified, functionalized and applied in biomedical fields such as PDT [229]. In a report of Dong and co-workers [230], MoS_2 QDs exhibited much superior $^1O_2$ production ability to a classic PS PpIX, implying great application potential for photodynamic therapy. Under irradiation of a 630 nm laser, the $^1O_2$ generation ability, detected by a chemical probe, was much stronger than PpIX. Besides, the $^1O_2$ production level assessed by a $^1O_2$ sensor green (SOSG) reagent also showed superior $^1O_2$ production ability of MoS_2 QDs to PpIX. It has been demonstrated that p–n heterostructures, which could absorb NIR light, could minimize side effect in PDT. Song et al. designed a theranostic nanoplatform with imaging-guided phototherapy. MoS_2 was employed to generate localized hyperthermia inside the tumor region to induce the PDT effect upon NIR excitation. At the meantime, MoS_2 was found to be an efficient PS as it could trigger massive ROS generation upon NIR-light irradiation. Yong [231] used H_2SO_4 intercalation and ultrasonication to construct WS_2 NSs with lower toxicity and better water solubility. Apart from acting as a NIR excitation agent for PTT, the WS_2 NSs could also act as a PS carrier for PDT, taking advantage of their ultra-large surface area to load PS. The $^1O_2$ production could be precisely adjusted by NIR light irradiation through manipulating the release behavior of PS. The synergistic anticancer effect was evaluated and the results revealed that the antitumor efficiency of PSs–WS_2 complex was much greater than those of PDT and PTT alone treatment.

9.4 Graphitic-phase carbon nitride (g-C_3N_4)

As a novel 2D layered nanomaterial with stacked 2D structure, graphitic carbon nitride (g-C_3N_4) NSs have displayed enormous potential as an excellent visible-light excited PS for PDT. Lin [232] first reported that g-C_3N_4 NSs could be employed as a potential PS for PDT as the *in vitro* experiment, in which a LED light source (wavelength of 440–450 nm) was used as light source, and showed that they could generate abundant ROS to kill the tumor cells effectively upon low-intensity light illumination (20 mW/cm^2). Ju [233] coordinated Cu^{2+} with 2D g-C_3N_4 and reported that the assembly of g-C_3N_4 and Cu^{2+} could enhance light-excited ROS generation and lower the intracellular levels of GSH, resulting in improved PDT efficacy. Moreover, Cu^{2+}–g-C_3N_4 could catalyze the H_2O_2 to hydroxyl radical and the reduction of molecular O_2 to superoxide anion, both of which contributed to the enhanced PDT efficiency. Chen [234] designed and developed core–shell NPs with g-C_3N_4 encapsulated by a zeolitic-imidazolate framework-8 (ZIF-8) shell. Within the NPs, the shell of ZIF-8 was used to deliver the chemotherapy agent Dox molecules, while the g-C3N4 NSs were visible-light excited PSs for PDT. The NPs could efficiently generate $^1O_2$ to destroy the tumor cells and deliver Dox with a pH-responsive release profile. Though Dox stacked on the NSs remained stable in the neutral buffer as only about 25% of the Dox was released into the pH 7.4 buffer after 70 hours, as much as about 85% of the Dox was released at pH 5.0 buffer, indicating that the NSs could be employed as efficient nanocarriers for Dox delivery that was pH-responsive. Results showed that the best antitumor effect was achieved in the group that the tumor cells were incubated with Dox-loaded NPs under irradiation of a xenon lamp with visible light. At the same concentration, the cell viability in group of Dox-loaded NPs with irradiation was as low as 16.6%, which showed significantly more cytotoxic than that of the Dox group and the irradiated nanoparticle group.

9.5 2D metal–organic frameworks (MOFs)

2D MOFs are formed by linking metal containing nods with organic ligands with crystalline porous structure [235]. On account of their tunable structures and ultra-large surface area, many efforts have been devoted to researching the biomedical application potential of 2D-MOF. Li [236] prepared the asymmetric UCNP-MOF heterodimers by anisotropic growth of Zr-based porphyrinic nanoscale MOFs onto the Lanthanide-doped UCNPs. The heterodimers could obtain photons beyond the nMOFs absorption spectrum by transferring resonance energy from UCNPs to nMOFs, thus promoting the generation of $^1O_2$ upon NIR light illumination. Besides, when loaded chemotherapeutic drug Dox into the porous channels of the nMOFs, the UCNP-MOF nanomaterials exhibited excellent antitumor effect. After NIR light irradiation, the cytotoxicity of Dox-loaded UCMOFs (Dox/UCMOFs) on tumor cells and the level of nuclear division and necrosis were much higher than the control group, indicating that the combined action of chemotherapy and NIR-induced PDT enhanced the therapeutic efficiency of UCMOFs. Zhu [237] fabricated 2D MOF-NSs using metal zinc cations (Zn^{2+}) and tetrakis (4-carboxyphenyl) porphyrin (TCPP), decorated with PEG for stability and bio-compatibility. The as-obtained 2D Zn-TCPP@PEG NSs exhibited distinctly better $^1O_2$ generation efficiency, compared to their particulate counterpart Zn-TCPP@PEG NPs with the same ingredient, under 660 nm light irradiation for enhanced PDT, and greater drug loading capacity (almost doubled) for Dox. The enhanced light-triggered $^1O_2$ generation ability and drug-loading capacity may be owing to the particular nano structure of the Zn-TCPP@PEG NSs with ultra-large surface area. *In vivo* inspecting showed an excellent synergistic anticancer efficiency of Zn-TCPP@PEG NSs upon light illumination. Lan [238] designed and synthesized two 2D metal–organic layers (MOLs), Hf-MOLs, which were composed of $[Hf_6O_4(OH)_4(HCO_2)_6]$ secondary building units (SBUs) and Ir[bpy(ppy)$_2$]$^+$- or [Ru(bpy)$_3$]$^{2+}$-derived tricarboxylate ligands, as PSs for PDT that could be induced by X-ray. Upon X-ray irradiation, the Hf-MOLs could generate sufficient $^1O_2$ effectively, demonstrated by both 4-nitroso-N,N-dimethylaniline (RNO) assay and SOSG assay. *In vivo* experiment showed a 90% reduction in tumor volumes upon X-ray irradiation, owing to high $^1O_2$ quantum yields and effective SO diffusion through 2D MOLs. Considering the excellent performance of MOF in the field of PDT, the researchers studied the effect of the MOF's thickness on the PDT performance. Jiang et al. fabricated 2D MOFs using a household microwave oven, and its thickness was controlled by changing the acetic acid concentration [239]. As the thickness decreases, the Brunauer–Emmett–Teller surface area, light harvesting ability, and light capture ability of the MOF increase significantly, which are beneficial for PDT. In addition,

thinner MOFs also exhibit slightly larger band gaps. What's more, the thinnest 2D MOFs also have the highest quantum yield (0.63) and the largest charge separation efficiency, which can promote the production of $^1O_2$. It is worth noting that this PS can produce not only $^1O_2$, but also O_2^-. In addition to thickness, researchers also studied the effect of metal node on the PDT. PSs containing Yb^{3+} show the best performance, probably due to the effective energy and electron transfer.

9.6 2D transition metal carbides and nitrides (MXenes)

Ti_3C_2 MXene is a novel 2DNM with various superb physicochemical and optical properties [240]. In Liu's report [241], they synthesized Ti_3C_2 MXene NSs with a highly steady surface functional group $Al(OH)_4-$ and a small lateral size. The Ti_3C_2 MXene NSs exhibited a splendid photothermal conversion efficiency of 58.3% and remarkable photodynamic potential under NIR light irradiation. Moreover, the Ti_3C_2 MXene NSs exhibited a glorious drug loading capacity of 84.2%. Based on the as-attained Ti_3C_2 MXene NSs, chemotherapy agent DOX and active tumor targeting agent hyaluronic acid were composited via layer-by-layer adsorption. The multifunctional Ti_3C_2 MXene based nano-platform was proved to be an excellent antitumor agent by *in vitro* and *in vivo* experiments, owing to the tumor targeting photothermal/photodynamic/chemo synergistic therapy.

9.7 2D layered double hydroxides (LDHs)

2D layered double hydroxides have been widely applied in the biomedicine applications on account of their unique properties such as controllable size and morphology, adaptability of chemical composition, better biocompatibility and highly chemical stability [242].

Guan [243] synthesized a ruthenium complex ($Ru(C\text{-}bpy)_2$) loaded monolayer LDH (mLDH) through electrostatic attraction between the opposite charges on mLDH and $Ru(C\text{-}bpy)_2$. Although $Ru(C\text{-}bpy)_2$ could produce photoelectron and photoholes upon light irradiation, the generated photoelectron and photoholes are readily to recombine with high efficiency. However, in this system, the existence of mLDH can greatly restrain the recombination of the photoelectron and photoholes, resulting in more electrons transported to mLDH and thereby produce $^1O_2$ more efficiently upon light irradiation. The results of electron spin resonance showed that the $^1O_2$ generation was dependent on the wavelength of light, as the $Ru(C\text{-}bpy)_2$/mLDH could produce $^1O_2$ with a high quantum yield upon 520 nm light irradiation while under 488 and 800 nm irradiation it could be as low as zero. Hematoxylin and eosin staining of the animals showed the severe necrosis of the tumor tissues after treatment by the $Ru(C\text{-}bpy)_2$/mLDH under 520 nm irradiation for 8 min. Some organic aromatic compounds existing in crystalline state can exhibit triplet-exciton emission with a long duration. Inspired by such a phenomenon, Gao [244] achieved long-lived triplet exciton by generating supramolecular PSs with different aromatic room temperature phosphorescence (RTP) molecules confined in 2D LDHs. The self-assembled PS based on 2D LDH, can be activated under 808 nm NIR irradiation for effective generation of $^1O_2$. Employing Rose Bengal (RB) as referential PS, the two-photon induced $^1O_2$ quantum yield generated from the supramolecular PSs isophthalic acid-LDH is estimated to be 0.74. The superior antitumor properties were confirmed by *in vitro* tests, as well as the extremely low toxicity and high biocompatibility.

9.8 Heterostructures based on 2DNMs

In PDT, there are two crucial processes. The first is to absorb light energy and achieve electron-hole pair separation. The second is to transfer energy to oxygen and produce ROS. Unfortunately, a narrow band gap is beneficial for the former, while a wide band gap is useful for the latter. To achieve a balance, Pan et al. designed a novel photosensitizer [245]. Modeled on the Z-scheme heterojunction in natural photosynthesis, this PS consists of FeS_2 core and Fe_2O_3 shell to form a heterojunction structure, which is called thermally oxidized pyrite NSs (TOPY NSs). Due to the unique Z-scheme heterojunction structure, photo-excited electrons in the conduction band of Fe_2O_3 can be transferred to the valence band of FeS_2. As a result, both FeS_2 cores and Fe_2O_3 in the TOPY NSs component can absorb photons independently, and realize electron-hole pair recombination between conduction band of FeS_2 and valence band of Fe_2O_3. In addition, TOPY NSs can also consume GSH to destroy the tumor microenvironment, and improve PDT efficacy.

9.9 Comparison of various 2DNMs

There are a lot of 2DNMs that have been prepared, many of which show unique advantages in PDT, as shown in Table 1. As the first exfoliated 2DNM, graphene has the most mature fabrication method and good dispersion in physiological environment. The delocalized π-electrons of graphene is conducive to bind various aromatic molecules through π-π stacking. GO and rGO, important graphene derivatives, also perform no worse than graphene in PDT application. With abundant functional groups on the surface, GO have various functional strategies and good dispersibility in physiological environment. In addition, with the development of fabrication methods, it is easy to obtain a large amount of GO, indicating broad clinical prospects. Tellurene is a non-layered 2DNM with wide applications in the field of PDT. With abundant surface dangling bonds, tellurene shows strong photocatalytic ability. As a result, good PDT effects have been confirmed by many works. However, the toxicity of tellurene deserves attention. Compared with tellurene or other 2DNMs, BP, a rising star in the biological field, possesses a relatively clear degradation mechanism. Under physiological environment, BPNSs can be completely degraded into phosphate, which is abundant in the body, distinguishing BP from other 2DNMs. In addition, the adjustable direct band gap of BP facilitates optical absorption. What's more, BP has a fairly high quantum yield to generate ROS. Due to puckered lattice configuration and lone pair electrons on surface, it is easy to load drugs or functionalize on the surface of BP. However, achieving a balance between long-acting treatment and suitable biodegradation is difficult. Fortunately, controllable degradation strategy may be a good solution. In addition, the biological effects of local enrichment of phosphates caused by the rapid BP degradation need further study. TMDs, another group of 2DNMs, have received wide attention. It also has unique advantages in PDT. Some TMDs have wide band gaps (such as MoS_2), which can transfer more energy to oxygen when the electron-hole pair recombines. In addition, the presence of sulfur is also conducive to the functionalization of TMDs. In the g-C_3N_4-related work, the negative impact of tumor microenvironment on PDT has been partly overcome. g-C_3N_4-based photosensitizers consume glutathione, which can reduce the toxicity of PDT. In addition, g-C_3N_4 can use H_2O_2 to produces •OH. Compared with the aforementioned 2DNMs, the structure and type of MOF are more complicated. The lanthanides in the MOF system make it possible to achieve NIR-induced PDT, which distinguishes MOF from other 2DNMs. The porous structure of some MOFs is beneficial for drug

Table 1 Performance of various 2DNMs PSs. Data are selected from papers with great performance

2D material	ROS type	quantum yield	Dose and light source *in vitro*	Dose and light source *in vivo*	Advantage	Ref.
Graphene	$^1O_2$	1.3	1.8 mM Xe lamp (6.5 mW/cm^2, 10 min)	4 mg/kg white light (80 mW/cm^2, 10 min irradiated twice)	Extremely high quantum yield; delocalized π-electrons	[28]
Graphdiyne	$^1O_2$		100 μg/mL 660 nm laser (0.5 W/cm^2, 10 min)	20.0 mg/kg 660 nm laser (0.5 W/cm^2, 10 min)	photocatalytic O_2 evolution	[46]
BP	$^1O_2$	0.91	0.2 μg/mL 660 nm laser (1 W/cm^2, 10 min)	30.0 μL, 500 μg/mL 660 nm laser (0.5 W/cm^2, 20 min)	Biodegradability	[25]
Tellurene	$^1O_2$		0.1 mM 670 nm laser (160 mW/cm^2, 10 min)	100 μL, 20 μg/mL 670 nm laser (160 mW/cm^2, 10 min)	Available for multispectral optoacoustic tomography	[8]
MoS_2	$^1O_2$		50 μg/mL 808 nm laser (0.8 W/cm^2, 10 min)	0.1 mg/mL, 100 μL 808 nm laser (0.8 W/ cm^2)	Remarkable up-conversion behavior	[246]
Heterojunction	$\cdot O_2^-$ and ·OH		100 μg/mL 808 nm laser (1 W/cm^2) and 650 nm laser (0.5 W/cm^2), 10 min	5 mg/kg 650 nm (0.5 W/cm^2) and 808 nm laser (1.0 W/cm^2), 10 min	Damaging the tumor microenvironment	[245]
MOFs	$^1O_2$, $\cdot O_2^-$		40 μg/mL 660 nm LED light (29.8 mW/ cm^2, 5 min)	1 mg/mL, 200 μL 660 nm laser (150 mW/cm^2)	NIR-induced PDT	[239]
Mxene (Ti_3C_2)	$^1O_2$		42 μg/mL 808 nm laser (0.8 W/cm^2, 10 min)	2.0 mg/kg 808 nm laser (0.8 W/cm^2, 10 min, 1–2 times)	NIR-induced PDT	[241]
g-C_3N_4			10 μg/mL 630 nm laser (40 mW/cm^2, 5 min)	2.5 mg/kg 630 nm laser (80 mW/cm^2, 10 min)	High photoluminescence (PL) quantum yields	[247]
LDHs	$^1O_2$	0.74	1 μg/mL 808 nm laser (1 W/cm^2, 5 min)	1 mg/kg 808 nm laser (0.7 W/cm^2, 10 min)	ultralong-lived triplet exciton	[244]

loading. Unfortunately, the diverse elemental composition brings not only advantages but also more risks to biosafety. Mxene has attracted widespread interest from researchers in recent years. Mxene shows great light absorption, unique surface plasmon enhancement effect, and heavy element related radiotherapy enhancement. With a unique etching-assisted liquid phase exfoliation method, the yield of Mxene is large. However, the existence of the fluorine element in the common method also determines that there a lot of works about biocompatibility to do before it can be implemented in clinical applications.

10.2 DNMs assisted PDT

Compared to the conventional PDT, 2DNMs can not only be used as a PS for the intrinsic PDT, but also as the deliverer and carrier of other PSs, PDT efficacy-improver and even targeting ligands.

Graphene-like 2D MoS_2 nanomaterials with particular optical property have been demonstrated to be promising photothermal agents for PTT on account of their outstanding photothermal energy conversion efficiency. Yang [248] prepared a multi-modal nanocomposites by constructing mesoporous silica nanorods with MoS_2 NSs coated for PTT, human serum albumin (HSA) conjugated for active targeting and classic PS Ce6 for PDT. Under the NIR laser irradiation, MoS_2 could efficiently induce hyperthermia and accelerate the release of Ce6, and thus dequenching Ce6 and promptly activating the PDT effect, achieving PTT/PDT synergetic therapy. Jia and co-workers [249] synthesized MoS_2 nanoplate-based nanocomposites to achieve ATP-controllable PDT. The AFM measurements showed the thickness around 0.9 nm of the MoS_2 nanoplates, suggesting the 2D layered structure of the MoS_2 nanoplates. Results showed that the MoS_2 nanoplates exhibited high loading efficiency of Ce6-aptamer. After the nanocomposites were absorbed and accumulated by ATP-rich lysosomes, the Ce6-aptamer would combine with ATP to form a folded rigid structure, leading to the release of Ce6-aptamer from MoS_2. The released PS Ce6 produced abundant $^1O_2$ under laser irradiation that induced cell death by the lysosomal pathway. Huang's team [250] designed FA-conjugated GO as target drug delivery system for Ce6 based PDT. In their report, the classic PS Ce6 was loaded onto GO through π-π stacking and hydrophobic interactions, sulfonic acid groups were decorated into GO to endow it with stability under physiological conditions, and FA were employed for targeting folate-receptor positive tumor cells. After bounding to the folate receptors, the FA-GO-Ce6 was endocytosed into cytoplasm to form endosomes, followed by turning into lysosomes, where Ce6 was released from FA-GO-Ce6 in the microenvironment of lysosomes to generate plenty $^1O_2$ under irradiation of He-Ne laser with 632.8 nm wavelength.

11 Challenges and future prospects

2D nanomaterials are characterized by possessing one dimension that is confined to single- or few-atoms thick, generally thinner than 5 nm. 2DNMs are considered as budding new class of materials and have attracted enormous interest across various scientific and technological disciplines, attributing to their particular characteristics like ultrahigh surface to volume ratio, broad optical absorption region, anisotropic structure and tunable functionalities [122, 251–254]. 2DNMs have been demonstrated to have exceptional potential in electrical, physiochemical, optical and biomedical applications. With unique electronic structure, many 2DNMs possess highly efficient yield of ROS, especially $^1O_2$, in the ultraviolet to entire visible region and even NIR region, which could be applied for photodynamic therapy. What's more, 2DNMs have been applied in PTT for a variety of cancers due to their NIR photothermal performance [255, 256]. Owing to an ultrahigh surface to volume ratio than 3D materials, 2DNMs proved to be superior to delivering agents like chemotherapy drugs and conventional PSs. The enormous specific surface areas and ultrahigh surface-

to-volume atom ratios also render easy contact with reactant molecules, thus amplifying the catalytic activities in catalysis. The various biomedical applications of 2DNMs include photothermal/photoacoustic/photodynamic therapy, biosensors, bio-imaging, drug delivery, theranostics, neuronal regeneration, and 3D printing. Despite possessing a number of superior properties in optics, electronics and physical chemistry, most 2DNMs have emerged for just a few years, and the exploration and development on 2DNMs is still in their infancy, so there still exists a considerable amount of challenges and also opportunities with regard to 2DNMs-based PDT for the actual use in clinical practice [257].

In general, nanoplatforms around 100 nm in size exhibit superior pharmacokinetics and vascular extravasation. Although smaller nanoplatforms are preferred for tumor penetration, they may be cleared out rapidly during blood circulation, resulting in inadequate tumor accumulation and lower antitumor efficiency. Extensive studies have shown that nanomaterials larger than 8 nm home to tumor tissues preferentially versus healthy tissues, because such nanomaterials can passively target tumors through inter-endothelial junctions (40 to 80 nm on average, and as large as 1 μm) that was larger than those of healthy tissues (≤ 8 nm) [258]. This passively targeting combined with defective lymphatic drainage could promote retention of such nanomaterials in tumor region. However, nanomaterials also suffer from being highly absorbed by mononuclear phagocyte system organs like liver and spleen, leading to inefficient clearance through hepatic excretion. Renal excretion is considered as the preferred clearance pathway to minimize the toxicity of nanomaterials. However, in general, only the spherical nanomaterials with a hydrodynamic diameter less than 6 nm can be readily cleared through glomerular capillary wall [259]. Therefore, it's obligatory to develop 2D nanomaterials with appropriate size that can endow them with passively targeting capacity and simultaneously rapid renal clearance for efficient killing effect of cancer cells without obvious toxicity to human body.

The biomedical applications of 2D nanomaterials were often restricted due to the vulnerability to ambient degradation. To take BP nanomaterials for example, owing to the existence of lone-pair electrons on the external layer of the P atom, BP nanomaterials are not stable in the presence of water, oxygen and light, particularly ultraviolet light. It can be easily degraded into phosphate groups, in which condition both the unique structure and prominent properties of BP would disappear rapidly, hindering its PDT efficacy in cancer therapy. Nonetheless, the poor ambient stability of BP nanomaterials may also be advantageous in tumor therapy [227], because BP can be degraded into biocompatible phosphorus oxides *in vivo* and thus avoiding long-term toxicity to human body after phototherapy. Hence, developing intelligent strategies to balance the stability and degradation of 2D nanomaterials are indispensable for successfully implementing PDT for malignant tumors and other biomedical applications.

Heterojunction construction is regarded as an effective method to attain the optimal photocatalytic performance of semiconductor. Recently, BP-based heterostructures have been designed out that not only greatly enhanced the stability in ambient condition but also induced mass production of $^1O_2$ upon light irradiation [36]. Kapri [260] developed PEG modified, MnO_2 nanoparticle decorated p-MoS_2/n-rGO NSs (p-MoS_2/n-rGO–MnO_2–PEG) to explore the potential of a nanoscale p–n heterojunction in PDT. Upon NIR light illumination (980 nm), the p-n heterojunction could promote the separation of charge carriers through enhancing the migration of electrons and holes [261], and thus increased the ROS production via photocatalysis, confirmed by the study showing the $^1O_2$ quantum yield of 37% in acetonitrile (CH_3CN)–D_2O solvent with respect to the standard PS Rose Bengal (0.76). By decorating MnO_2 particle, the obtained NSs overcame the hypoxic conditions in the cellular microenvironment through catalyzing endogenous H_2O_2 efficiently to generate enough O_2. *In vitro* experiments demonstrated the enhanced PDT efficacy of p-MoS_2/n-rGO–MnO_2–PEG NSs via a mechanism of inducing apoptosis of cancer cells. Up to now, there are several drawbacks for the traditional single-modal cancer therapies, such as low efficiency, poor target specificity, and systematic or organ toxicity. Combined therapy approach may be the most promising way to address these issues due to its high antitumor efficacy and low risk of recurrence. It is still a main challenge, although numerous strategies have been tried, to develop multifunctional nanomaterials with higher synergistic combination therapy effect.

Until now, thousands of cases of PDT in clinical practice have been reported worldwide, among which dozens of cancers have been treated, such as lung cancer, bladder cancer, rectal cancer and cholangiocarcinoma. A large number of studies have shown that PDT has achieved some success in the treatment of cholangiocarcinoma. At 2017, a meta-analysis [262] about PDT for unresectable cholangiocarcinoma was conducted to evaluate its impact on the survival, including 10 clinical studies involving 402 patients, in which PS was mainly Photofrin. Results showed that the median survival time was 413 days in the PDT plus biliary stent drainage group compared with 183 days in the biliary stent drainage group. Cheon et al. [263] conducted a retrospective clinical study on PDT to determine the long-term outcome of PDT with biliary stenting (BS) compared with BS alone in patients with advanced hilar cholangiocarcinoma. There are two main approaches to insert the laser fiber into the bile duct to irradiate the tumor. One is through percutaneous transhepatic cholangioscopy (PTCS). The laser fiber was inserted into the guiding catheter to irradiate the stricture sites from distal to proximal region guided by the cholangioscopy and fluoroscopy. The other approach is through endoscopic retrograde cholangiopancreatography (ERCP). The PDT fiber was inserted across the bile duct tumor using a guidewire and the tumor segments were treated from the proximal to the distal. They reported that the application of the first-generation PS Photofrin in PDT with biliary drainage treatment (72 cases) significantly extended the median survival time compared with the biliary drainage treatment (71 cases) (9.8 months vs. 7.3 months $P = 0.029$). Multivariate analysis confirmed that PDT combined with biliary drainage was an important predictor of survival. Gonzalez-Carmona et al. [264] evaluated the benefit of PDT combined with chemotherapy compared to chemotherapy alone in patients with advanced extrahepatic cholangiocarcinoma. In this study, the photosensitizing agent used included the porphyrin derivates Photosan or Photofrin, or the chlorine derivate Foscan. The agent was injected intravenously one to two days prior to PDT and PDT was performed by the way of ERCP. Results showed that combined PDT with chemotherapy had significantly longer OS than chemotherapy alone ($P = 0.022$). The median survival in the combination group was 20 months, 15 months in PDT group and 10 months in the chemotherapy group. In multivariate analysis, combination therapy and PDT alone were both independent predictors of longer survival. Lung cancer remains one of the most virulent cancers threatening lives of all mankind. Although the standard treatment for lung cancer is radical resection, many of the patients are often poor surgical candidates. Therefore, palliative intervention was often required. Kimura [265] presented clinical data of 12 patients with advanced

non-small cell lung carcinoma with airway stenosis who were not suitable for radical operation. They underwent PDT combined with chemotherapy (titanium silicate or platinum-doublet) for local treatment of the intraluminal lesions. The PS was talaporfin sodium, a water-soluble second-generation PS. At this study, the median and mean survival time was 5.9 and 9.3 months, respectively, and the overall 1-year survival rate was 30%. As the procedure was very safe and non-invasive, no PDT-related morbidity or mortality appeared. Besides, they had improved symptoms and quality of life.

PDT has been conformed highly effective in treating malignant skin lesions, and can also be applied in the treatment of head and neck tumors, lung cancer, esophageal cancer, nasopharyngeal cancer and so on. However, many patients are relatively unresponsive to PDT, leading to not so satisfactory efficacy of PDT. To take our previous clinical study of PDT for cholangiocarcinoma for instance, although most patients were relieved of bile duct obstruction after PDT treatment, with improved quality of life and extended survival period, there were still about 30% of patients that could not obtain any benefit (biliary obstruction was not relieved, quality of life was not improved, and survival period was not prolonged) from PDT. There may be two reasons for this phenomenon: First, the presently used PS in clinical practice has a low yield of $^1O_2$ and a limited killing effect on cancer cells. Second, the severe hypoxia condition in the tumor microenvironment. With versatile properties, 2DNMs-based nanocomposite may be the key to work out the above practical problems. On the one hand, apply 2DNMs like BP to efficiently generate $^1O_2$ to solve the problem of insufficient tumor-killing efficacy of PS. On the other hand, assemble 2DNMs with oxygen-supporting group like MnO_2 to catalyze H_2O_2 in the tumor region for production of O_2 to alleviate the hypoxic condition of the microenvironment. Combining the above two aspects may be conducive to maximizing the potential of PDT in the treatment of cholangiocarcinoma and other PDT-recalcitrant cancers.

Although there have been not any clinical trials that prove higher antitumor efficiency of 2DNMs-based PDT than traditional PDT, many ongoing or completed clinical trials employing nano-structured materials can provide us the way forward. Autio et al. performed a phase II clinical trial to assess the safety and effectiveness of BIND-014, a nanoparticle that contained chemotherapeutic agent docetaxel and PSMA-targeted, for metastatic castration-resistant prostate cancer (mCRPC) [266]. Results displayed that the median progression-free survival was about 10 months, the number of circulating tumor cells (CTCs) were notably reduced, and the untoward events were mainly grade 1 or 2 fatigue, nausea, and diarrhea. This clinical trial suggested that the nanostructured agent BIND-014 was safe and effective in patients with mCRPC. EPR effect of nanomaterials has been verified in animal models, but its extent and discrepancy in human tumors is still controversial. ^{64}Cu-MM-302, A ^{64}Cu-labeled nanoparticle, was utilized by Lee et al. to evaluate the EPR effect in patients with metastatic breast cancer by positron emission tomography and computed tomography (PET/CT) [267]. Data revealed that the concentration of ^{64}Cu-MM-302 in tumor region varied 35-fold at 24 to 48 h after administration, and that high concentration of ^{64}Cu-MM-302 inside tumor was correlated with better treatment outcomes. Wollina et al. conducted a prospective trial using a nano-emulsified 5-aminolevulinic acid (5-ALA) for PDT to treat field cancerization caused by ultraviolet light exposure upon red light irradiation [268]. Clinical data showed 93.3% of the patients achieved complete clearance, and the remaining patients achieved more than 90% clearance without systemic toxicity, which were significantly better than classical local treatment with diclofenac gel. Therefore, nanostructured medicines can be well tolerated to we humans, and their specific characteristics promise to overcome variable physicochemical conditions of the tumor environment and greatly improve prognosis of various kinds of cancer.

Although PDT is considered as a promising modality to cure various malignant caner diseases, there are still issues need to be addressed. Multifunctional system combining clear diagnostic imaging and efficient therapy will be crucial in the near future. The employment of 2D nanomaterials seems to be a rational strategy. With unique electronic structure and exceptional optical properties, 2DNMs are expected to conquer any obstacle in maximizing antitumor efficacy of therapies including PDT.

Acknowledgement

The research was partially supported by the National Natural Science Fundation of China (Nos. 61875138, 61435010, and 61961136001), and Science and Technology Innovation Commission of Shenzhen (No. JCYJ20170811093453105). Authors also acknowledge the support from Instrumental Analysis Center of Shenzhen University (Xili Campus).

Conflict of interest

The authors declare no conflict of interest.

References

[1] Chilakamarthi, U.; Giribabu, L. Photodynamic therapy: Past, present and future. *Chem. Rec.* **2017**, *17*, 775–802.

[2] Zhang, J.; Jiang, C. S.; Figueiró Longo, J. P.; Azevedo, R. B.; Zhang, H.; Muehlmann, L. A. An updated overview on the development of new photosensitizers for anticancer photodynamic therapy. *Acta Pharm. Sin. B* **2018**, *8*, 137–146.

[3] Kwiatkowski, S.; Knap, B.; Przystupski, D.; Saczko, J.; Kędzierska, E.; Knap-Czop, K.; Kotlińska, J.; Michel, O.; Kotowski, K.; Kulbacka, J. Photodynamic therapy-mechanisms, photosensitizers and combinations. *Biomed. Pharmacother.* **2018**, *106*, 1098–1107.

[4] Zhang, K.; Zhang, Y. D.; Meng, X. D.; Lu, H. T.; Chang, H.; Dong, H. F.; Zhang, X. J. Light-triggered theranostic liposomes for tumor diagnosis and combined photodynamic and hypoxia-activated prodrug therapy. *Biomaterials* **2018**, *185*, 301–309.

[5] Theodoraki, M. N.; Lorenz, K.; Lotfi, R.; Fürst, D.; Tsamadou, C.; Jaekle, S.; Mytilineos, J.; Brunner, C.; Theodorakis, J.; Hoffmann, T. K. et al. Influence of photodynamic therapy on peripheral immune cell populations and cytokine concentrations in head and neck cancer. *Photodiagnosis Photodyn. Ther.* **2017**, *19*, 194–201.

[6] Kochevar, I. E. Singlet oxygen signaling: From intimate to global. *Sci. STKE* **2004**, *2004*, pe7.

[7] Wang, H.; Jiang, S. L.; Shao, W.; Zhang, X. D.; Chen, S. C.; Sun, X. S.; Zhang, Q.; Luo, Y.; Xie, Y. Optically switchable photocatalysis in ultrathin black phosphorus nanosheets. *J. Am. Chem. Soc.* **2018**, *140*, 3474–3480.

[8] Lin, Y.; Wu, Y.; Wang, R.; Tao, G.; Luo, P. F.; Lin, X.; Huang, G. M.; Li, J.; Yang, H. H. Two-dimensional tellurium nanosheets for photoacoustic imaging-guided photodynamic therapy. *Chem. Commun.* **2018**, *54*, 8579–8582.

[9] Duan, X. P.; Chan, C.; Guo, N. N.; Han, W. B.; Weichselbaum, R. R.; Lin, W. B. Photodynamic therapy mediated by nontoxic core-shell nanoparticles synergizes with immune checkpoint blockade to elicit antitumor immunity and antimetastatic effect on breast cancer. *J. Am. Chem. Soc.* **2016**, *138*, 16686–16695.

[10] Pizova, K.; Tomankova, K.; Daskova, A.; Binder, S.; Bajgar, R.; Kolarova, H. Photodynamic therapy for enhancing antitumour immunity. *Biomed. Pap.* **2012**, *156*, 93–102.

[11] Yeung, H. Y.; Lo, P. C.; Ng, D. K. P.; Fong, W. P. Anti-tumor immunity of BAM-SiPc-mediated vascular photodynamic therapy in a BALB/c mouse model. *Cell. Mol. Immunol.* **2017**, *14*, 223–234.

[12] Wang, T. T.; Zhang, H.; Han, Y. B.; Liu, H. H.; Ren, F.; Zeng, J. F.; Sun, Q.; Li, Z.; Gao, M. Y. Light-enhanced O_2-evolving nanoparticles boost photodynamic therapy to elicit antitumor immunity. *ACS Appl. Mater. Interfaces* **2019**, *11*, 16367–16379.
[13] Jin, R. M.; Yang, J.; Ding, P. C.; Li, C. Q.; Zhang, B.; Chen, W.; Zhao, Y. D.; Cao, Y. C.; Liu, B. Antitumor Immunity triggered by photothermal therapy and photodynamic therapy of a 2D MoS_2 nanosheet-incorporated injectable polypeptide-engineered hydrogel combinated with chemotherapy for 4T1 breast tumor therapy. *Nanotechnology* **2020**, *31*, 205102.
[14] Tsubone, T. M.; Martins, W. K.; Pavani, C.; Junqueira, H. C.; Itri, R.; Baptista, M. S. Enhanced efficiency of cell death by lysosome-specific photodamage. *Sci. Rep.* **2017**, *7*, 6734.
[15] van Lith, S. A. M.; van den Brand, D.; Wallbrecher, R.; Wübbeke, L.; van Duijnhoven, S. M. J.; Mäkinen, P. I.; Hoogstad-van Evert, J. S.; Massuger, L.; Ylä-Herttuala, S.; Brock, R. et al. The effect of subcellular localization on the efficiency of EGFR-targeted VHH photosensitizer conjugates. *Eur. J. Pharm. Biopharm.* **2018**, *124*, 63–72.
[16] Martins, W. K.; Santos, N. F.; de Sousa Rocha, C.; Bacellar, I. O. L.; Tsubone, T. M.; Viotto, A. C.; Matsukuma, A. Y.; De P. Abrantes, A. B.; Siani, P.; Dias, L. G. et al. Parallel damage in mitochondria and lysosomes is an efficient way to photoinduce cell death. *Autophagy* **2019**, *15*, 259–279.
[17] Huang, J.; Zong, C.; Shen, H.; Liu, M.; Chen, B.; Ren, B.; Zhang, Z. J. Mechanism of cellular uptake of graphene oxide studied by surface-enhanced Raman spectroscopy. *Small* **2012**, *8*, 2577–2584.
[18] Zhao, H. N.; Zhang, W.; Liu, Z. M.; Huang, D. Q.; Zhang, W. L.; Ye, B. G.; Hu, G. S.; Zhong, H. Q.; Zhuang, Z. F.; Guo, Z. Y. Insights into the intracellular behaviors of black-phosphorus-based nanocomposites via surface-enhanced Raman spectroscopy. *Nanophotonics* **2018**, *7*, 1651–1662.
[19] Zhu, X. B.; Ji, X. Y.; Kong, N.; Chen, Y. H.; Mahmoudi, M.; Xu, X. D.; Ding, L.; Tao, W.; Cai, T.; Li, Y. J. et al. Intracellular mechanistic understanding of 2D MoS_2 nanosheets for anti-exocytosis-enhanced synergistic cancer therapy. *ACS Nano* **2018**, *12*, 2922–2938.
[20] Yang, T.; Ke, H. T.; Wang, Q. L.; Tang, Y. A.; Deng, Y. B.; Yang, H.; Yang, X. L.; Yang, P.; Ling, D. S.; Chen, C. Y. et al. Bifunctional tellurium nanodots for photo-induced synergistic cancer therapy. *ACS Nano* **2017**, *11*, 10012–10024.
[21] Mao, J.; Chen, P. Y.; Liang, J. S.; Guo, R. H.; Yan, L. T. Receptor-mediated endocytosis of two-dimensional nanomaterials undergoes flat vesiculation and occurs by revolution and self-rotation. *ACS Nano* **2016**, *10*, 1493–1502.
[22] Tao, W.; Ji, X. Y.; Zhu, X. B.; Li, L.; Wang, J. Q.; Zhang, Y.; Er Saw, P.; Li, W. L.; Kong, N.; Islam, M. A. et al. Two-dimensional antimonene-based photonic nanomedicine for cancer theranostics. *Adv. Mater.* **2018**, *30*, e1802061.
[23] Song, Y. F.; Shi, X. J.; Wu, C. F.; Tang, D. Y.; Zhang, H. Recent progress of study on optical solitons in fiber lasers. *Appl. Phys. Rev.* **2019**, *6*, 021313.
[24] Matsumoto, J.; Suzuki, K.; Yasuda, M.; Yamaguchi, Y.; Hishikawa, Y.; Imamura, N.; Nanashima, A. Photodynamic therapy of human biliary cancer cell line using combination of phosphorus porphyrins and light emitting diode. *Bioorg. Med. Chem.* **2017**, *25*, 6536–6541.
[25] Wang, H.; Yang, X. Z.; Shao, W.; Chen, S. C.; Xie, J. F.; Zhang, X. D.; Wang, J.; Xie, Y. Ultrathin black phosphorus nanosheets for efficient singlet oxygen generation. *J. Am. Chem. Soc.* **2015**, *137*, 11376–11382.
[26] Guo, T.; Wu, Y.; Lin, Y.; Xu, X.; Lian, H.; Huang, G. M.; Liu, J. Z.; Wu, X. P.; Yang, H. H. Black phosphorus quantum dots with renal clearance property for efficient photodynamic therapy. *Small* **2018**, *14*, 1702815.
[27] Idris, N. M.; Gnanasammandhan, M. K.; Zhang, J.; Ho, P. C.; Mahendran, R.; Zhang, Y. *In vivo* photodynamic therapy using upconversion nanoparticles as remote-controlled nanotransducers. *Nat. Med.* **2012**, *18*, 1580–1585.
[28] Ge, J. C.; Lan, M. H.; Zhou, B. J.; Liu, W. M.; Guo, L.; Wang, H.; Jia, Q. Y.; Niu, G. L.; Huang, X.; Zhou, H. Y. et al. A graphene quantum dot photodynamic therapy agent with high singlet oxygen generation. *Nat. Commun.* **2014**, *5*, 4596.
[29] Zheng, X. L.; Ge, J. C.; Wu, J. S.; Liu, W. M.; Guo, L.; Jia, Q. Y.; Ding, Y.; Zhang, H. Y.; Wang, P. F. Biodegradable hypocrellin derivative nanovesicle as a near-infrared light-driven theranostic for dually photoactive cancer imaging and therapy. *Biomaterials* **2018**, *185*, 133–141.
[30] Dibaba, S. T.; Wei, R. Y.; Xi, W. S.; Zhao, L.; Shi, L. Y.; Ren, W.; Mayr, T.; Sun, L. N. Theranostic nanocomposite from upconversion luminescent nanoparticles and black phosphorus nanosheets. *RSC Adv.* **2018**, *8*, 35706–35718.
[31] Hamblin, M. R. Upconversion in photodynamic therapy: Plumbing the depths. *Dalton Trans.* **2018**, *47*, 8571–8580.
[32] Wang, C.; Cheng, L.; Liu, Z. Upconversion nanoparticles for photodynamic therapy and other cancer therapeutics. *Theranostics* **2013**, *3*, 317–330.
[33] Liu, Y. Y.; Liu, Y.; Bu, W. B.; Cheng, C.; Zuo, C. J.; Xiao, Q. F.; Sun, Y.; Ni, D. L.; Zhang, C.; Liu, J. N. et al. Hypoxia induced by upconversion-based photodynamic therapy: towards highly effective synergistic bioreductive therapy in tumors. *Angew. Chem., Int. Ed.* **2015**, *54*, 8105–8109.
[34] Lv, R. C.; Yang, D.; Yang, P. P.; Xu, J. T.; He, F.; Gai, S. L.; Li, C. X.; Dai, Y. L.; Yang, G. X.; Lin, J. Integration of upconversion nanoparticles and ultrathin black phosphorus for efficient photodynamic theranostics under 808 nm near-infrared light irradiation. *Chem. Mater.* **2016**, *28*, 4724–4734.
[35] Hu, J.; Tang, Y. A.; Elmenoufy, A. H.; Xu, H. B.; Cheng, Z.; Yang, X. L. Nanocomposite-based photodynamic therapy strategies for deep tumor treatment. *Small* **2015**, *11*, 5860–5887.
[36] Huang, H.; He, L. Z.; Zhou, W. H.; Qu, G. B.; Wang, J. B.; Yang, N.; Gao, J.; Chen, T. F.; Chu, P. K.; Yu, X. F. Stable black phosphorus/Bi_2O_3 heterostructures for synergistic cancer radiotherapy. *Biomaterials* **2018**, *171*, 12–22.
[37] Detty, M. R.; Gibson, S. L.; Wagner, S. J. Current clinical and preclinical photosensitizers for use in photodynamic therapy. *J. Med. Chem.* **2004**, *47*, 3897–3915.
[38] Tang, X. L.; Cheng, Y. H.; Huang, S. T.; Zhi, F.; Yuan, A. H.; Hu, Y. Q.; Wu, J. H. Overcome the limitation of hypoxia against photodynamic therapy to treat cancer cells by using perfluorocarbon nanodroplet for photosensitizer delivery. *Biochem. Biophys. Res. Commun.* **2017**, *487*, 483–487.
[39] Liu, J. T.; Du P; Liu, T. R.; Córdova Wong, B. J.; Wang, W. P.; Ju, H. X.; Lei, J. P. A black phosphorus/manganese dioxide nanoplatform: Oxygen self-supply monitoring, photodynamic therapy enhancement and feedback. *Biomaterials* **2019**, *192*, 179–188.
[40] Casas, A.; Di Venosa, G.; Hasan, T.; Batlle, A. Mechanisms of resistance to photodynamic therapy. *Curr. Med. Chem.* **2011**, *18*, 2486–2515.
[41] Cadamuro, M.; Stecca, T.; Brivio, S.; Mariotti, V.; Fiorotto, R.; Spirli, C.; Strazzabosco, M.; Fabris, L. The deleterious interplay between tumor epithelia and stroma in cholangiocarcinoma. *Biochim. Biophys. Acta* (*BBA*) *Mol. Basis Dis.* **2018**, *1864*, 1435–1443.
[42] Liu, J. T.; Du P; Mao, H.; Zhang, L.; Ju, H. X.; Lei, J. P. Dual-triggered oxygen self-supply black phosphorus nanosystem for enhanced photodynamic therapy. *Biomaterials* **2018**, *172*, 83–91.
[43] Ma, Z. F.; Zhang, M. C.; Jia, X. D.; Bai, J.; Ruan, Y. D.; Wang, C.; Sun, X. P.; Jiang, X. Fe^{III}-doped two-dimensional C_3N_4 nanofusiform: A new O_2-evolving and mitochondria-targeting photodynamic agent for MRI and enhanced antitumor therapy. *Small* **2016**, *12*, 5477–5487.
[44] Ouyang, J.; Deng, Y. Y.; Chen, W. S.; Xu, Q. F.; Wang, L. Q.; Liu, Z. J.; Tang, F. Y.; Deng, L.; Liu, Y. N. Marriage of artificial catalase and black phosphorus nanosheets for reinforced photodynamic antitumor therapy. *J. Mater. Chem. B* **2018**, *6*, 2057–2064.
[45] Lan, S. Y.; Lin, Z. G.; Zhang, D.; Zeng, Y. Y.; Liu, X. L. Photocatalysis enhancement for programmable killing of hepatocellular carcinoma through self-compensation mechanisms based on black phosphorus quantum-dot-hybridized nanocatalysts. *ACS Appl. Mater. Interfaces* **2019**, *11*, 9804–9813.
[46] Jiang, W.; Zhang, Z.; Wang, Q.; Dou, J. X.; Zhao, Y. Y.; Ma, Y. C.; Liu, H. R.; Xu, H. R.; Wang, Y. C. Tumor reoxygenation and blood perfusion enhanced photodynamic therapy using ultrathin graphdiyne oxide nanosheets. *Nano Lett.* **2019**, *19*, 4060–4067.
[47] Zhang, C.; Ren, J.; Hua, J. S.; Xia, L. Y.; He, J.; Huo, D.; Hu, Y. Multifunctional Bi_2WO_6 nanoparticles for CT-guided photothermal and oxygen-free photodynamic therapy. *ACS Appl. Mater. Interfaces* **2018**, *10*, 1132–1146.

[48] Ge, X. X.; Xia, Z. H.; Guo, S. J. Recent advances on black phosphorus for biomedicine and biosensing. *Adv. Funct. Mater.* **2019**, *29*, 1900318.
[49] Luo, M. M.; Fan, T. J.; Zhou, Y.; Zhang, H.; Mei, L. 2D black phosphorus-based biomedical applications. *Adv. Funct. Mater.* **2019**, *29*, 1808306.
[50] Walia, S.; Balendhran, S.; Ahmed, T.; Singh, M.; El-Badawi, C.; Brennan, M. D.; Weerathunge, P.; Karim, M. N.; Rahman, F.; Rassell, A. et al. Ambient protection of few-layer black phosphorus via sequestration of reactive oxygen species. *Adv. Mater.* **2017**, *29*, 1700152.
[51] Zhou, Q. H.; Chen, Q.; Tong, Y. L.; Wang, J. L. Light-induced ambient degradation of few-layer black phosphorus: Mechanism and protection. *Angew. Chem., Int. Ed.* **2016**, *55*, 11437–11441.
[52] Favron, A.; Gaufrès, E.; Fossard, F.; Phaneuf-L'Heureux, A. L.; Tang, N. Y. W.; Lévesque, P. L.; Loiseau, A.; Leonelli, R.; Francoeur, S.; Martel, R. Photooxidation and quantum confinement effects in exfoliated black phosphorus. *Nat. Mater.* **2015**, *14*, 826–832.
[53] Qiu, M.; Wang, D.; Liang, W. Y.; Liu, L. P.; Zhang, Y.; Chen, X.; Sang, D. K.; Xing, C. Y.; Li, Z. J.; Dong, B. Q. et al. Novel concept of the smart NIR-light-controlled drug release of black phosphorus nanostructure for cancer therapy. *Proc. Natl. Acad. Sci. USA* **2018**, *115*, 501–506.
[54] Liu, H.; Zhang, Y.; Dong, Y. P.; Chu, X. F. Electrogenerated chemiluminescence aptasensor for lysozyme based on copolymer nanospheres encapsulated black phosphorus quantum dots. *Talanta* **2019**, *199*, 507–512.
[55] Chen, L.; Chen, C.; Chen, W.; Li, K.; Chen, X. Z.; Tang, X. D.; Xie, G. F.; Luo, X.; Wang, X. J.; Liang, H. J. et al. Biodegradable black phosphorus nanosheets mediate specific delivery of hTERT siRNA for synergistic cancer therapy. *ACS Appl. Mater. Interfaces* **2018**, *10*, 21137–21148.
[56] Liu, T.; Wang, C.; Cui, W.; Gong, H.; Liang, C.; Shi, X. Z.; Li, Z. W.; Sun, B. Q.; Liu, Z. Combined photothermal and photodynamic therapy delivered by PEGylated MoS_2 nanosheets. *Nanoscale* **2014**, *6*, 11219–11225.
[57] Gao, N. S.; Nie, J. P.; Wang, H. F.; Xing, C. Y.; Mei, L.; Xiong, W.; Zeng, X. W.; Peng, Z. C. A versatile platform based on black phosphorus nanosheets with enhanced stability for cancer synergistic therapy. *J. Biomed. Nanotechnol.* **2018**, *14*, 1883–1897.
[58] Liu, Y. L.; Zhou, M.; Zhang, W. C.; Chen, K. Q.; Mei, A. H.; Zhang, Y. Y.; Chen, W. Enhanced photocatalytic properties of TiO_2 nanosheets@2D layered black phosphorus composite with high stability under hydro-oxygen environment. *Nanoscale* **2019**, *11*, 5674–5683.
[59] Zhang, Z. C.; He, D. Y.; Liu, H. Y.; Ren, M.; Zhang, Y. N.; Qu, J.; Lu, N.; Guan, J. N.; Yuan, X. Synthesis of graphene/black phosphorus hybrid with highly stable P-C bond towards the enhancement of photocatalytic activity. *Environ. Pollut.* **2019**, *245*, 950–956.
[60] Xing, B. R.; Guan, L.; Yu, Y.; Niu, X. Y.; Yan, X. Y.; Zhang, S. C.; Yao, J. D.; Wang, D.; Sha, J.; Wang, Y. W. HfO_2-Passivated black phosphorus field effect transistor with long-termed stability and enhanced current on/off ratio. *Nanotechnology* **2019**, *30*, 345208.
[61] Yang, B. C.; Wan, B. S.; Zhou, Q. H.; Wang, Y.; Hu, W. T.; Lv, W. M.; Chen, Q.; Zeng, Z. M.; Wen, F. S.; Xiang, J. Y. et al. Te-doped black phosphorus field-effect transistors. *Adv. Mater.* **2016**, *28*, 9408–9415.
[62] Lv, W. M.; Yang, B. C.; Wang, B. C.; Wan, W. H.; Ge, Y. F.; Yang, R. L.; Hao, C. X.; Xiang, J. Y.; Zhang, B. S.; Zeng, Z. M. et al. Sulfur-doped black phosphorus field-effect transistors with enhanced stability. *ACS Appl. Mater. Interfaces* **2018**, *10*, 9663–9668.
[63] Li, H.; Lian, P. C.; Lu, Q. J.; Chen, J. C.; Hou, R. R.; Mei, Y. Excellent air and water stability of two-dimensional black phosphorene/MXene heterostructure. *Mater. Res. Express* **2016**, *6*, 65504.
[64] Cai, J. Y.; Gou, X. D.; Sun, B. L.; Li, W. Y.; Li, D.; Liu, J. L.; Hu, F. D.; Li, Y. D. Porous graphene-black phosphorus nanocomposite modified electrode for detection of leptin. *Biosens. Bioelectron.* **2019**, *137*, 88–95.
[65] Iyer, A. K.; Khaled, G.; Fang, J.; Maeda, H. Exploiting the enhanced permeability and retention effect for tumor targeting. *Drug Discov. Today* **2006**, *11*, 812–818.
[66] Sun, Z. B.; Zhao, Y. T.; Li, Z. B.; Cui, H. D.; Zhou, Y. Y.; Li, W. H.; Tao, W.; Zhang, H.; Wang, H. Y.; Chu, P. K. et al. TiL_4-coordinated black phosphorus quantum dots as an efficient contrast agent for *in vivo* photoacoustic imaging of cancer. *Small* **2017**, *13*, 1602896.
[67] Chan, L.; Gao, P.; Zhou, W. H.; Mei, C. M.; Huang, Y. Y.; Yu, X. F.; Chu, P. K.; Chen, T. F. Sequentially triggered delivery system of black phosphorus quantum dots with surface charge-switching ability for precise tumor radiosensitization. *ACS Nano* **2018**, *12*, 12401–12415.
[68] Wan, H.; Zhang, Y.; Zhang, W. B.; Zou, H. F. Robust two-photon visualized nanocarrier with dual targeting ability for controlled chemo-photodynamic synergistic treatment of cancer. *ACS Appl. Mater. Interfaces* **2015**, *7*, 9608–9618.
[69] Li, Z.; Guo, T.; Hu, Y. H.; Qiu, Y.; Liu, Y.; Wang, H. M.; Li, Y.; Chen, X.; Song, J. B.; Yang, H. H. A Highly effective π–π stacking strategy to modify black phosphorus with aromatic molecules for cancer theranostics. *ACS Appl. Mater. Interfaces* **2019**, *11*, 9860–9871.
[70] Luo, M. M.; Cheng, W.; Zeng, X. W.; Mei, L.; Liu, G.; Deng, W. B. Folic acid-functionalized black phosphorus quantum dots for targeted chemo-photothermal combination cancer therapy. *Pharmaceutics* **2019**, *11*, 242.
[71] Wei, Y. C.; Zhou, F. F.; Zhang, D.; Chen, Q.; Xing, D. A graphene oxide based smart drug delivery system for tumor mitochondria-targeting photodynamic therapy. *Nanoscale* **2016**, *8*, 3530–3538.
[72] Wang, Y. W.; Qiu, M.; Won, M.; Jung, E.; Fan, T. J.; Xie, N.; Chi, S. G.; Zhang, H.; Kim, J. S. Emerging 2D material-based nanocarrier for cancer therapy beyond graphene. *Coordin. Chem. Rev.* **2019**, *400*, 213041.
[73] Wang, Z. T.; Mu, H. R.; Yuan, J.; Zhao, C. J.; Bao, Q. L.; Zhang, H. Graphene-Bi_2Te_3 heterostructure as broadband saturable absorber for ultra-short pulse generation in Er-doped and Yb-doped fiber lasers. *IEEE J. Sel. Top. Quant. Electron.* **2017**, *23*, 8800105.
[74] Song, Y. F.; Liang, Z. M.; Zhang, H.; Zhang, Q.; Zhao, L. M.; Shen, D. Y.; Tang, D. Y. Period-doubling and quadrupling bifurcation of vector soliton bunches in a graphene mode locked fiber laser. *IEEE Photonics J.* **2017**, *9*, 4502308.
[75] Liu, S. X.; Li, Z. J.; Ge, Y. Q.; Wang, H. D.; Yue, R.; Jiang, X. T.; Li, J. Q.; Wen, Q.; Zhang, H. Graphene/phosphorene nano-heterojunction: Facile synthesis, nonlinear optics, and ultrafast photonics applications with enhanced performance. *Photonics Res.* **2017**, *5*, 662–668.
[76] Chen, X.; Wang, Y.; Xiang, Y. J.; Jiang, G. B.; Wang, L. L.; Bao, Q. L.; Zhang, H.; Liu, Y.; Wen, S. C.; Fan, D. Y. A broadband optical modulator based on a graphene hybrid plasmonic waveguide. *J. Lightwave Technol.* **2016**, *34*, 4948–4953.
[77] Ponraj, J. S.; Xu, Z. Q.; Dhanabalan, S. C.; Mu, H. R.; Wang, Y. S.; Yuan, J.; Li, P. F.; Thakur, S.; Ashrafi, M.; McCoubrey, K. et al. Photonics and optoelectronics of two-dimensional materials beyond graphene. *Nanotechnology* **2016**, *27*, 462001.
[78] Loh, K. P.; Bao, Q. L.; Eda, G.; Chhowalla, M. Graphene oxide as a chemically tunable platform for optical applications. *Nat. Chem.* **2010**, *2*, 1015–1024.
[79] Dreyer, D. R.; Park, S.; Bielawski, C. W.; Ruoff, R. S. The chemistry of graphene oxide. *Chem. Soc. Rev.* **2009**, *39*, 228–240.
[80] Paredes, J. I.; Villar-Rodil, S.; Martínez-Alonso, A.; Tascón, J. M. D. Graphene oxide dispersions in organic solvents. *Langmuir* **2008**, *24*, 10560–10564.
[81] Stankovich, S.; Dikin, D. A.; Piner, R. D.; Kohlhaas, K. A.; Kleinhammes, A.; Jia, Y. Y.; Yue, W.; Nguyen, S. B. T.; Ruoff, R. S. Synthesis of graphene-based nanosheets via chemical reduction of exfoliated graphite oxide. *Carbon* **2007**, *45*, 1558–1565.
[82] Zhou, M.; Zhai, Y. M.; Dong, S. J. Electrochemical sensing and biosensing platform based on chemically reduced graphene oxide. *Anal. Chem.* **2009**, *81*, 5603–5613.
[83] Zhou, Y.; Bao, Q. L.; Tang, L. A. L.; Zhong, Y. L.; Loh, K. P. Hydrothermal dehydration for the "Green" reduction of exfoliated graphene oxide to graphene and demonstration of tunable optical limiting properties. *Chem. Mater.* **2009**, *21*, 2950–2956.
[84] Li, X. L.; Wang, H. L.; Robinson, J. T.; Sanchez, H.; Diankov, G.; Dai, H. J. Simultaneous nitrogen doping and reduction of graphene oxide. *J. Am. Chem. Soc.* **2009**, *131*, 15939–15944.
[85] Eda, G.; Fanchini, G.; Chhowalla, M. Large-area ultrathin films of reduced graphene oxide as a transparent and flexible electronic material. *Nat. Nanotechnol.* **2008**, *3*, 270–274.
[86] Williams, G.; Seger, B.; Kamat, P. V. TiO_2-graphene nanocomposites.

UV-assisted photocatalytic reduction of graphene oxide. *ACS Nano* **2008**, *2*, 1487–1491.

[87] Wu, L. M.; Xie, Z. J.; Lu, L.; Zhao, J. L.; Wang, Y. Z.; Jiang, X. T.; Ge, Y. Q.; Zhang, F.; Lu, S. B.; Guo, Z. N. et al. Few-layer tin sulfide: A promising black-phosphorus-analogue 2D material with exceptionally large nonlinear optical response, high stability, and applications in all-optical switching and wavelength conversion. *Adv. Opt. Mater.* **2018**, *6*, 1700985.

[88] Xue, Y.; Xie, Z. D.; Ye, Z. L.; Hu, X. P.; Xu, J. L.; Zhang, H. Enhanced saturable absorption of MoS_2 black phosphorus composite in 2 μm passively Q-switched Tm:YAP laser. *Chin. Opt. Lett.* **2018**, *16*, 020018.

[89] Sharma, A.; Wen, B.; Liu, B. Q.; Myint, Y. W.; Zhang, H.; Lu, Y. R. Defect engineering in few-layer phosphorene. *Small* **2018**, *14*, 1704556.

[90] Zhou, J.; Li, Z. J.; Ying, M.; Liu, M. X.; Wang, X. M.; Wang, X. Y.; Cao, L. W.; Zhang, H.; Xu, G. X. Black phosphorus nanosheets for rapid microRNA detection. *Nanoscale* **2018**, *10*, 5060–5064.

[91] Luo, S. J.; Zhao, J. L.; Zou, J. F.; He, Z. L.; Xu, C. W.; Liu, F. W.; Huang, Y.; Dong, L.; Wang, L.; Zhang, H. Self-standing polypyrrole/black phosphorus laminated film: Promising electrode for flexible supercapacitor with enhanced capacitance and cycling stability. *ACS Appl. Mater. Interfaces* **2018**, *10*, 3538–3548.

[92] Zhang, C. L.; Li, Y. L.; Zhang, P. X.; Qiu, M.; Jiang, X. T.; Zhang, H. Antimonene quantum dot-based solid-state solar cells with enhanced performance and high stability. *Sol. Energy Mater. Sol. Cells* **2019**, *189*, 11–20.

[93] Xue, T. Y.; Liang, W. Y.; Li, Y. W.; Sun, Y. H.; Xiang, Y. J.; Zhang, Y. P.; Dai, Z. G.; Duo, Y. H.; Wu, L. M.; Qi, K. et al. Ultrasensitive detection of miRNA with an antimonene-based surface plasmon resonance sensor. *Nat. Commun.* **2019**, *10*, 28.

[94] Song, Y. F.; Chen, Y. X.; Jiang, X. T.; Liang, W. Y.; Wang, K.; Liang, Z. M.; Ge, Y. Q.; Zhang, F.; Wu, L. M.; Zheng, J. L. et al. Nonlinear few-layer antimonene-based all-optical signal processing: Ultrafast optical switching and high-speed wavelength conversion. *Adv. Opt. Mater.* **2018**, *6*, 1701287.

[95] Feng, B. J.; Sugino, O.; Liu, R. Y.; Zhang, J.; Yukawa, R.; Kawamura, M.; Iimori, T.; Kim, H.; Hasegawa, Y.; Li, H. et al. Dirac fermions in borophene. *Phys. Rev. Lett.* **2017**, *118*, 096401.

[96] Mannix, A. J.; Zhou, X. F.; Kiraly, B.; Wood, J. D.; Alducin, D.; Myers, B. D.; Liu, X. L.; Fisher, B. L.; Santiago, U.; Guest, J. R. et al. Synthesis of borophenes: Anisotropic, two-dimensional boron polymorphs. *Science* **2016**, *350*, 1513–1516.

[97] Feng, B. J.; Zhang, J.; Zhong, Q.; Li, W. B.; Li, S.; Li, H.; Cheng, P.; Meng, S.; Chen, L.; Wu, K. H. Experimental realization of two-dimensional boron sheets. *Nat. Chem.* **2016**, *8*, 563–568.

[98] Peng, B.; Zhang, H.; Shao, H. Z.; Xu, Y. F.; Zhang, R. J.; Zhu, H. Y. The electronic, optical, and thermodynamic properties of borophene from first-principle calculations. *J. Mater. Chem. C* **2016**, *4*, 3592–3598.

[99] Wang, H. F.; Li, Q. F.; Gao, Y.; Miao, F.; Zhou, X. F.; Wan, X. G. Strain effects on borophene: Ideal strength, negative Possion's ratio and phonon instability. *New J. Phys.* **2016**, *18*, 073016.

[100] Li, W. L.; Chen, Q.; Tian, W. J.; Bai, H.; Zhao, Y. F.; Hu, H. S.; Li, J.; Zhai, H. J.; Li, S. D.; Wang, L. S. The B35 cluster with a double-hexagonal vacancy: A new and more flexible structural motif for borophene. *J. Am. Chem. Soc.* **2014**, *136*, 12257–12260.

[101] Meng, L.; Wang, Y. L.; Zhang, L. Z.; Du, S. X.; Wu, R. T.; Li, L. F.; Zhang, Y.; Li, G.; Zhou, H. T.; Hofer, W. et al. A. Buckled silicene formation on Ir(111). *Nano Lett.* **2013**, *13*, 685–690.

[102] Fleurence, A.; Friedlein, R.; Ozaki, T.; Kawai, H.; Wang, Y.; Yamada-Takamura, Y. Experimental evidence for epitaxial silicene on diboride thin films. *Phys. Rev. Lett.* **2012**, *108*, 245501.

[103] Feng, B. J.; Ding, Z. J.; Meng, S.; Yao, Y. G.; He, X. Y.; Peng, C.; Lan, C.; Wu, K. H. Evidence of silicene in honeycomb structures of silicon on Ag(111). *Nano Lett.* **2012**, *12*, 3507–3511.

[104] Liu, C. C.; Feng, W. X.; Yao, Y. G. Quantum spin Hall effect in silicene and two-dimensional germanium. *Phys. Rev. Lett.* **2011**, *107*, 076802.

[105] Lalmi, B.; Oughaddou, H.; Enriquez, H.; Kara, A.; Vizzini, S.; Ealet, B.; Aufray, B. Epitaxial growth of a silicene sheet. *Appl. Phys. Lett.* **2010**, *97*, 223109.

[106] Balendhran, S.; Walia, S.; Nili, H.; Sriram, S.; Bhaskaran, M. Elemental analogues of graphene: Silicene, germanene, stanene, and phosphorene. *Small* **2015**, *11*, 640–652.

[107] Li, L. F.; Lu, S. Z.; Pan, J. B.; Qin, Z. H.; Wang, Y. Q.; Wang, Y. L.; Cao, G. Y.; Du, S. X.; Gao, H. J. ChemInform abstract: Buckled germanene formation on Pt(111). *Cheminform* **2015**, *45*, 4820–4824.

[108] Dávila, M. E.; Xian, L.; Cahangirov, S.; Rubio, A.; Le Lay, G. Germanene: A novel two-dimensional Germanium allotrope akin to Graphene and Silicene. *New J. Phys.* **2014**, *16*, 095002.

[109] Ni, Z. Y.; Liu, Q. H.; Tang, K. C.; Zheng, J. X.; Zhou, J.; Qin, R.; Gao, Z. X.; Yu, D. P.; Lu, J. Tunable bandgap in silicene and germanene. *Nano Lett.* **2012**, *12*, 113–118.

[110] Houssa, M.; Scalise, E.; Sankaran, K.; Pourtois, G.; Afanas'ev, V. V.; Stesmans, A. Electronic properties of hydrogenated silicene and germanene. *Appl. Phys. Lett.* **2011**, *98*, 223107.

[111] Peng, B.; Zhang, H.; Shao, H. Z.; Xu, Y. C.; Zhang, X. C.; Zhu, H. Y. Low lattice thermal conductivity of stanene. *Sci. Rep.* **2016**, *6*, 20225.

[112] Zhu, F. F.; Chen, W. J.; Xu, Y.; Gao, C. L.; Guan, D. D.; Liu, C. H.; Qian, D.; Zhang, S. C.; Jia, J. F. Epitaxial growth of two-dimensional stanene. *Nat. Mater.* **2015**, *14*, 1020–1025.

[113] Zhang, R. W.; Zhang, C. W.; Ji, W. X.; Li, S. S.; Hu, S. J.; Yan, S. S.; Li, P.; Wang, P. J.; Li, F. Ethynyl-functionalized stanene film: A promising candidate as large-gap quantum spin Hall insulator. *New J. Phys.* **2015**, *17*, 083036.

[114] Xu, Y.; Tang, P. Z.; Zhang, S. C. Large-gap quantum spin hall states in decorated stanene grown on a substrate. *Phys. Rev. B* **2015**, *92*, 081112(R).

[115] Wang, Y. P.; Ji, W. X.; Zhang, C. W.; Li, P.; Li, F.; Ren, M. J.; Chen, X. L.; Yuan, M.; Wang, P. J. Controllable band structure and topological phase transition in two-dimensional hydrogenated arsenene. *Sci. Rep.* **2016**, *6*, 20342.

[116] Pizzi, G.; Gibertini, M.; Dib, E.; Marzari, N.; Iannaccone, G.; Fiori, G. Performance of arsenene and antimonene double-gate MOSFETs from first principles. *Nat. Commun.* **2016**, *7*, 12585.

[117] Zhang, S. L.; Yan, Z.; Li, Y. F.; Chen, Z. F.; Zeng, H. B. Atomically thin arsenene and antimonene: Semimetal-semiconductor and indirect-direct band-gap transitions. *Angew. Chem., Int. Ed.* **2015**, *127*, 3155–3158.

[118] Zhang, H. J.; Ma, Y. D.; Chen, Z. F. Quantum spin hall insulators in strain-modified arsenene. *Nanoscale* **2015**, *7*, 19152–19159.

[119] Zhang, S. L.; Hu, Y. H.; Hu, Z. Y.; Cai, B.; Zeng, H. B. Hydrogenated arsenenes as planar magnet and Dirac material. *Appl. Phys. Lett.* **2015**, *107*, 022102.

[120] Wang, Y. L.; Ding, Y. Electronic structure and carrier mobilities of arsenene and antimonene nanoribbons: A first-principle study. *Nanoscale Res. Lett.* **2015**, *10*, 254.

[121] Huang, H.; Ren, X. H.; Li, Z. J.; Wang, H. D.; Huang, Z. Y.; Qiao, H.; Tang, P. H.; Zhao, J. L.; Liang, W. Y.; Ge, Y. Q. et al. Two-dimensional bismuth nanosheets as prospective photo-detector with tunable optoelectronic performance. *Nanotechnology* **2018**, *29*, 235201.

[122] Guo, B.; Wang, S. H.; Wu, Z. X.; Wang, Z. X.; Wang, D. H.; Huang, H.; Zhang, F.; Ge, Y. Q.; Zhang, H. Sub-200 fs soliton mode-locked fiber laser based on bismuthene saturable absorber. *Opt. Express* **2018**, *26*, 22750–22760.

[123] Lu, L.; Liang, Z. M.; Wu, L. M.; Chen, Y. X.; Song, Y. F.; Dhanabalan, S. C.; Ponraj, J. S.; Dong, B. Q.; Xiang, Y. J.; Xing, F. et al. Few-layer bismuthene: Sonochemical exfoliation, nonlinear optics and applications for ultrafast photonics with enhanced stability. *Laser Photonics Rev.* **2018**, *12*, 1700221.

[124] Liu, J. J.; Huang, H.; Zhang, F.; Zhang, Z.; Liu, J.; Zhang, H.; Su, L. B. Bismuth nanosheets as a Q-switcher for a mid-infrared erbium-doped SrF_2 laser. *Photonics Res.* **2018**, *6*, 762–767.

[125] Xing, C. Y.; Huang, W. C.; Xie, Z. J.; Zhao, J. L.; Ma, D. T.; Fan, T. J.; Liang, W. Y.; Ge, Y. Q.; Dong, B. Q.; Li, J. Q. et al. Ultrasmall bismuth quantum dots: Facile liquid-phase exfoliation, characterization, and application in high-performance UV–Vis photodetector. *ACS Photonics* **2018**, *5*, 621–629.

[126] Jiang, Y. Q; Miao, L. L.; Jiang, G. B.; Chen, Y.; Qi, X.; Jiang, X. F.; Zhang, H.; Wen, S. C. Broadband and enhanced nonlinear optical response of MoS_2/graphene nanocomposites for ultrafast photonics

applications. *Sci. Rep.* **2015**, *5*, 16372.
[127] Huang, Z. Y.; Han, W. J.; Tang, H. L.; Ren, L.; Chander, D. S.; Qi, X.; Zhang, H. Photoelectrochemical-type sunlight photodetector based on MoS_2/graphene heterostructure. *2D Mater.* **2015**, *2*, 035011.
[128] Splendiani, A.; Sun, L.; Zhang, Y. B.; Li, T. S.; Kim, J.; Chim, C. Y.; Galli, G.; Wang, F. Emerging photoluminescence in monolayer MoS_2. *Nano Lett.* **2010**, *10*, 1271–1275.
[129] Lee, C.; Yan, H. G.; Brus, L. E.; Heinz, T. F.; Hone, J.; Ryu, S. Anomalous lattice vibrations of single- and few-layer MoS_2. *ACS Nano* **2010**, *4*, 2695–2700.
[130] Zong, X.; Yan, H. J.; Wu, G. P.; Ma, G. J.; Wen, F. Y.; Wang, L.; Li, C. Enhancement of photocatalytic H_2 evolution on CdS by loading MoS_2 as cocatalyst under visible light irradiation. *J. Am. Chem. Soc.* **2008**, *130*, 7176–7177.
[131] Feldman, Y.; Wasserman, E.; Srolovitz, D. J.; Tenne, R. High-rate, gas-phase growth of MoS_2 nested inorganic fullerenes and nanotubes. *Science* **1995**, *267*, 222–225.
[132] Ge, Y. Q.; Zhu, Z. F.; Xu, Y. H.; Chen, Y. X.; Chen, S.; Liang, Z. M.; Song, Y. F.; Zou, Y. S.; Zeng, H. B.; Xu, S. X. et al. Broadband nonlinear photoresponse of 2D TiS_2 for ultrashort pulse generation and all-optical thresholding devices. *Adv. Opt. Mater.* **2018**, *6*, 1701166.
[133] Zeng, Z. Y.; Tan, C. L.; Huang, X.; Bao, S. Y.; Zhang, H. Growth of noble metal nanoparticles on single-layer TiS_2 and TaS_2 nanosheets for hydrogen evolution reaction. *Energy Environ. Sci.* **2014**, *7*, 797–803.
[134] Lin, C. W.; Zhu, X. J.; Feng, J.; Wu, C. Z.; Hu, S. L.; Peng, J.; Guo, Y. Q.; Peng, L. L.; Zhao, J. Y.; Huang, J. L. Hydrogen-incorporated TiS_2 ultrathin nanosheets with ultrahigh conductivity for stamp-transferrable electrodes. *J. Am. Chem. Soc.* **2013**, *135*, 5144–5151.
[135] Li, C. T.; Lee, C. P.; Li, Y. Y.; Yeh, M. H.; Ho, K. C. A composite film of TiS_2/PEDOT:PSS as the electrocatalyst for the counter electrode in dye-sensitized solar cells. *J. Mater. Chem. A* **2013**, *1*, 14888–14896.
[136] Guilmeau, E.; Bréard, Y.; Maignan, A. Transport and thermoelectric properties in Copper intercalated TiS2 chalcogenide. *Appl. Phys. Lett.* **2011**, *99*, 052107.
[137] Chen, S. Y.; Wang, Z. X.; Fang, X. P.; Zhao, H. L.; Liu, X. J.; Chen, L. Q. Characterization of TiS_2 as an anode material for lithium Ion batteries. *Acta Phys. -Chim. Sin.* **2011**, *27*, 97–102.
[138] Navarro-Moratalla, E.; Island, J. O.; Mañas-Valero, S.; Pinilla-Cienfuegos, E.; Castellanos-Gomez, A.; Quereda, J.; Rubio-Bollinger, G.; Chirolli, L.; Silva-Guillén, J. A.; Agraït, N. Enhanced superconductivity in atomically thin TaS_2. *Nat. Commun.* **2016**, *7*, 11043.
[139] Li, H.; Lu, G.; Wang, Y. L.; Yin, Z. Y.; Cong, C. X.; He, Q. Y.; Wang, L.; Ding, F.; Yu, T.; Zhang, H. Mechanical exfoliation and characterization of single- and few-layer nanosheets of WSe_2, TaS_2, and $TaSe_2$. *Small* **2013**, *9*, 1974–1981.
[140] Coronado, E.; Forment-Aliaga, A.; Navarro-Moratalla, E.; Pinilla-Cienfuegos, E.; Castellanos-Gomez, A. Nanofabrication of TaS_2 conducting layers nanopatterned with Ta_2O_5 insulating regions via AFM. *J. Mater. Chem. C* **2013**, *1*, 7692–7694.
[141] Gao, Y.; Liu, Z. B.; Sun, D. M.; Huang, L.; Ma, L. P.; Yin, L. C.; Ma, T.; Zhang, Z. Y.; Ma, X. L.; Peng, L. M. et al. Large-area synthesis of high-quality and uniform monolayer WS_2 on reusable Au foils. *Nat. Commun.* **2015**, *6*, 8569.
[142] Georgiou, T.; Jalil, R.; Belle, B. D.; Britnell, L.; Gorbachev, R. V.; Morozov, S. V.; Kim, Y. J.; Gholinia, A.; Haigh, S. J.; Makarovsky, O. et al. Vertical field-effect transistor based on graphene-WS_2 heterostructures for flexible and transparent electronics. *Nat. Nanotechnol.* **2013**, *8*, 100–103.
[143] Zhao, W. J.; Ghorannevis, Z.; Chu, L. Q.; Toh, M.; Kloc, C.; Tan, P. H.; Eda, G. Evolution of electronic structure in atomically thin sheets of WS_2 and WSe_2. *ACS Nano* **2013**, *7*, 791–797.
[144] Rapoport, L.; Bilik, Y.; Feldman, Y.; Homyonfer, M.; Cohen, S. R. Hollow nanoparticles of WS_2 as potential solid-state lubricants. *Nature* **2012**, *387*, 791–793.
[145] Ramakrishna Matte, H. S. S.; Gomathi, A.; Manna, A. K.; Late, D. J.; Datta, R.; Pati, S. K.; Rao, C. N. R. MoS_2 and WS_2 analogues of graphene. *Angew. Chem., Int. Ed.* **2010**, *49*, 4059–4062.
[146] Ho, W.; Yu, J. C.; Lin, J.; Yu, J. G.; Li, P. Preparation and photocatalytic behavior of MoS_2 and WS_2 nanocluster sensitized TiO_2. *Langmuir* **2004**, *20*, 5865–5869.
[147] Huang, C. M.; Wu, S. F.; Sanchez, A. M.; Peters, J. J. P.; Beanland, R.; Ross, J. S.; Rivera, P.; Yao, W.; Cobden, D. H.; Xu, X. D. Lateral heterojunctions within monolayer $MoSe_2$-WSe_2 semiconductors. *Nat. Mater.* **2014**, *13*, 1096–1101.
[148] Wang, X. L.; Gong, Y. J.; Shi, G.; Chow, W. L.; Keyshar, K.; Ye, G. L.; Vajtai, R.; Lou, J.; Liu, Z.; Ringe, E. et al. Chemical vapor deposition growth of crystalline monolayer $MoSe_2$. *ACS Nano* **2014**, *8*, 5125–5131.
[149] Lu, X.; Utama, M. I. B.; Lin, J. H.; Gong, X.; Zhang, J.; Zhao, Y. Y.; Pantelides, S. T.; Wang, J. X.; Dong, Z. L.; Liu, Z. et al. Large-area synthesis of monolayer and few-layer $MoSe_2$ films on SiO_2 substrates. *Nano Lett.* **2014**, *14*, 2419–2425.
[150] Tonndorf, P.; Schmidt, R.; Böttger, P.; Zhang, X.; Börner, J.; Liebig, A.; Albrecht, M.; Kloc, C.; Gordan, O.; Zahn, D. R. T. et al. Photoluminescence emission and Raman response of MoS_2, $MoSe_2$, and WSe_2 nanolayers. *Opt. Express*, **2013**, *21*, 4908–4916.
[151] Kubart, T.; Polcar, T.; Kopecký, L.; Novák, R.; Nováková, D. Temperature dependence of tribological properties of MOS_2 and $MoSe_2$ coatings. *Surf. Coat. Technol.* **2005**, *193*, 230–233.
[152] Huang, J. K.; Pu, J.; Hsu, C. L.; Chiu, M. H.; Juang, Z. Y.; Chang, Y. H.; Chang, W. H.; Iwasa, Y.; Takenobu, T.; Li, L. J. Large-area synthesis of highly crystalline WSe_2 monolayers and device applications. *ACS Nano* **2014**, *8*, 923–930.
[153] Das, S.; Appenzeller, J. WSe_2 field effect transistors with enhanced ambipolar characteristics. *Appl. Phys. Lett.* **2013**, *103*, 103501.
[154] Fang, H.; Chuang, S.; Chang, T. C.; Takei, K.; Takahashi, T.; Javey, A. High-performance single layered WSe_2 p-FETs with chemically doped contacts. *Nano Lett.* **2012**, *12*, 3788–3792.
[155] Chiritescu, C.; Cahill, D. G.; Nguyen, N.; Johnson, D.; Bodapati, A.; Keblinski, P.; Zschack, P. Ultralow thermal conductivity in disordered, layered WSe_2 crystals. *Science* **2007**, *315*, 351–353.
[156] Zhi, C. Y.; Bando, Y.; Tang, C. C.; Kuwahara, H.; Golberg, D. Large-scale fabrication of boron nitride nanosheets and their utilization in polymeric composites with improved thermal and mechanical properties. *Adv. Mater.* **2009**, *21*, 2889–2893.
[157] Anasori, B.; Lukatskaya, M. R.; Gogotsi, Y. 2D metal carbides and nitrides (MXenes) for energy storage. *Nat. Rev. Mater.* **2017**, *2*, 16098.
[158] Anasori, B.; Xie, Y.; Beidaghi, M.; Lu, J.; Hosler, B. C.; Hultman, L.; Kent, P. R. C.; Gogotsi, Y.; Barsoum, M. W. Two-dimensional, ordered, double transition metals carbides (MXenes). *ACS Nano* **2015**, *9*, 9507–9516.
[159] Naguib, M.; Mochalin, V. N.; Barsoum, M. W.; Gogotsi, Y. 25th anniversary article: MXenes: A new family of two-dimensional materials. *Adv. Mater.* **2014**, *26*, 992–1005.
[160] Lukatskaya, M. R.; Mashtalir, O.; Ren, C. E.; Dall'Agnese, Y.; Rozier, P.; Taberna, P. L.; Naguib, M.; Simon, P.; Barsoum, M. W.; Gogotsi, Y. Cation intercalation and high volumetric capacitance of two-dimensional titanium carbide. *Science* **2013**, *341*, 1502–1505.
[161] Tang, Q.; Zhou, Z.; Shen, P. W. Are MXenes promising anode materials for Li ion batteries? Computational studies on electronic properties and Li storage capability of Ti_3C_2 and $Ti_3C_2X_2$ (X = F, OH) monolayer. *J. Am. Chem. Soc.* **2012**, *134*, 16909–16916.
[162] Zhang, X. D.; Xie, X.; Wang, H.; Zhang, J. J.; Pan, B. C.; Xie, Y. Enhanced photoresponsive ultrathin graphitic-phase C_3N_4 nanosheets for bioimaging. *J. Am. Chem. Soc.* **2013**, *135*, 18–21.
[163] Pan, C. S.; Xu, J.; Wang, Y. J.; Li, D.; Zhu, Y. F. Dramatic activity of C_3N_4/$BiPO_4$ Photocatalyst with core/shell structure formed by self-assembly. *Adv. Funct. Mater.* **2012**, *22*, 1518–1524.
[164] Ge, L.; Han, C. C.; Liu, J. Novel visible light-induced g-C_3N_4/Bi_2WO_6 composite photocatalysts for efficient degradation of methyl orange. *Appl. Catal. B: Environ.* **2011**, *108–109*, 100–107.
[165] Dong, F.; Wu, L. W.; Sun, Y. J.; Min, F. J.; Wu, Z. B.; Lee, S. C. Efficient synthesis of polymeric g-C_3N_4 layered materials as novel efficient visible light driven photocatalysts. *J. Mater. Chem.* **2011**, *21*, 15171–15174.
[166] Yan, S. C.; Li, Z. S.; Zou, Z. G. Photodegradation performance of g-C_3N_4 fabricated by directly heating melamine. *Langmuir* **2009**, *25*, 10397–10401.
[167] Osada, M.; Sasaki, T. Exfoliated oxidenanosheets: New solution to

nanoelectronics. *J. Mater. Chem.* **2009**, *19*, 2503–2511.
[168] Wang, Q.; O'Hare, D. Recent advances in the synthesis and application of layered double hydroxide (LDH) nanosheets. *Chem. Rev.* **2012**, *112*, 4124–4155.
[169] Xing, C. Y.; Xie, Z. J.; Liang, Z. M.; Liang, W. Y.; Fan, T. J.; Ponraj, J. S.; Dhanabalan, S. C.; Fan, D. Y.; Zhang, H. 2D nonlayered selenium nanosheets: Facile synthesis, photoluminescence, and ultrafast photonics. *Adv. Opt. Mater.* **2017**, *5*, 1700884.
[170] Tang, X.; Liang, W. Y.; Zhao, J. L.; Li, Z. J.; Qiu, M.; Fan, T. J.; Luo, C. S.; Zhou, Y.; Li, Y.; Guo, Z. N. et al. Fluorinated phosphorene: Electrochemical synthesis, atomistic fluorination, and enhanced stability. *Small* **2017**, *13*, 1702739.
[171] Wang, H. D.; Sang, D. K.; Guo, Z. N.; Cao, R.; Zhao, J. L.; Ullah Shah, M. N.; Fan, T. J.; Fan, D. Y.; Zhang, H. Black phosphorus-based field effect transistor devices for Ag ions detection. *Chinese Phys. B* **2018**, *27*, 087308.
[172] Jiang, X. T.; Gross, S.; Withford, M. J.; Zhang, H.; Yeom, D. I.; Rotermund, F.; Fuerbach, A. Low-dimensional nanomaterial saturable absorbers for ultrashort-pulsed waveguide lasers. *Opt. Mater. Express* **2018**, *8*, 3055–3071.
[173] Ge, Y. Q.; Liang, Z. M.; Chen, Y. X.; Song, Y. F.; Li, L.; Zhang, H.; Zhao, L. M.; Fan, D. Y. Characterization of dark soliton sidebands in all-normal-dispersion fiber lasers. *IEEE J. Sel. Top. Quant. Electron.* **2018**, *24*, 0903407.
[174] Tuo, M. F.; Xu, C.; Mu, H. R.; Bao, X. Z.; Wang, Y. W.; Xiao, S.; Ma, W. L.; Li, L.; Tang, D. Y.; Zhang, H. et al. Ultrathin 2D transition metal carbides for ultrafast pulsed fiber lasers. *ACS Photonics* **2018**, *5*, 1808–1816.
[175] Liu, J. J.; Liu, J.; Guo, Z. N.; Zhang, H.; Ma, W. W.; Wang, J. Y.; Su, L. B. Dual-wavelength Q-switched Er:SrF2 laser with a black phosphorus absorber in the mid-infrared region. *Opt. Express* **2016**, *24*, 30289–30295.
[176] Yao, Z.; Jiao, Y.; Ge, L.; Jaroniec, M.; Qiao, S. Z. Two-step boron and nitrogen doping in graphene for enhanced synergistic catalysis. *Angew, Chem., Int. Ed.* **2013**, *52*, 3110–3116.
[177] Lukowski, M. A.; Daniel, A. S.; Meng, F.; Forticaux, A.; Li, L. S.; Jin, S. Enhanced hydrogen evolution catalysis from chemically exfoliated metallic MoS_2 nanosheets. *J. Am. Chem. Soc.* **2013**, *135*, 10274–10277.
[178] Huang, X.; Zeng, Z. Y.; Bao, S. Y.; Wang, M. F.; Qi, X. Y.; Fan, Z. X.; Zhang, H. Solution-phase epitaxial growth of noble metal nanostructures on dispersible single-layer molybdenum disulfide nanosheets. *Nat. Commun.* **2013**, *4*, 1444.
[179] Qu, L. T.; Liu, Y.; Baek, J. B.; Dai, L. M. Nitrogen-doped graphene as efficient metal-free electrocatalyst for oxygen reduction in fuel cells. *ACS Nano* **2010**, *4*, 1321–1326.
[180] Zhu, J. X.; Yang, D.; Yin, Z. Y.; Yan, Q. Y.; Zhang, H. Graphene and graphene-based materials for energy storage applications. *Small* **2014**, *10*, 3480–3498.
[181] Yin, Z. Y.; Zhu, J. X.; He, Q. Y.; Cao, X. H.; Tan, C. L.; Chen, H. Y.; Yan, Q. Y.; Zhang, H. Graphene-based materials for solar cell applications. *Adv. Energy Mater.* **2014**, *4*, 1300574.
[182] Yang, X. W.; Cheng, C.; Wang, Y. F..; Qiu, L.; Li, D. Liquid-mediated dense integration of graphene materials for compact capacitive energy storage. *Science* **2013**, *341*, 534–537.
[183] Yoo, E. J.; Kim, J.; Hosono, E.; Zhou, H. S.; Kudo, T.; Honma, I. Large reversible Li storage of graphene nanosheet families for use in rechargeable lithium ion batteries. *Nano Lett.* **2008**, *8*, 2277–2282.
[184] Ding, H. J.; Shu, X. L.; Jin, Y. K.; Fan, T. J.; Zhang, H. Recent advances in nanomaterial-enabled acoustic devices for audible sound generation and detection. *Nanoscale* **2019**, *11*, 5839–5860.
[185] Fan, T. J.; Zhou, Y. S.; Qiu, M.; Zhang, H. Black phosphorus: A novel nanoplatform with potential in the field of bio-photonic nanomedicine. *J. Innov. Opt. Health Sci.* **2018**, *11*, 1830003.
[186] Li, H.; Wu, J.; Yin, Z. Y.; Zhang, H. Preparation and applications of mechanically exfoliated single-layer and multilayer MoS_2 and WSe_2 nanosheets. *Acc. Chem. Res.* **2014**, *47*, 1067–1075.
[187] Dean, C. R.; Young, A. F.; Meric, I.; Lee, C.; Wang, L.; Sorgenfrei, S.; Watanabe, K.; Taniguchi, T.; Kim, P.; Shepard, K. L. et al. Boron nitride substrates for high-quality graphene electronics. *Nat. Nanotechnol.* **2010**, *5*, 722–726.
[188] Goyal, V.; Teweldebrhan, D.; Balandin, A. A. Mechanically-exfoliated stacks of thin films of Bi_2Te_3 topological insulators with enhanced thermoelectric performance. *Appl. Phys. Lett.* **2010**, *97*, 133117.
[189] Novoselov, K. S.; Jiang, D.; Schedin, F.; Booth, T. J.; Khotkevich, V. V.; Morozov, S. V.; Geim, A. K. Two-dimensional atomic crystals. *Proc. Natl. Acad. Sci. USA* **2005**, *102*, 10451–10453.
[190] Xing, C. Y.; Chen, S. Y.; Qiu, M.; Liang, X.; Liu, Q.; Zou, Q. S.; Li, Z. J.; Xie, Z. J.; Wang, D.; Dong, B. Q. et al. Conceptually novel black phosphorus/cellulose hydrogels as promising photothermal agents for effective cancer therapy. *Adv. Healthc. Mater.* **2018**, *7*, 1701510.
[191] Kafaei, N.; Beiranvand, K.; Sabaeian, M.; Ghalambor Dezfuli, A.; Zhang, H. Spin-dependent k. p Hamiltonian of black phosphorene based on Löwdin partitioning method. *J. Appl. Phys.* **2018**, *124*, 035702.
[192] Liu, J. M.; Chen, Y.; Li, Y.; Zhang, H.; Zheng, S. Q.; Xu, S. X. Switchable dual-wavelength Q-switched fiber laser using multilayer black phosphorus as a saturable absorber. *Photonics Res.* **2018**, *6*, 198–203.
[193] Wang, Y. Z.; Zhang, F.; Tang, X.; Chen, X.; Chen, Y. X.; Huang, W. C.; Liang, Z. M.; Wu, L. M.; Ge, Y. Q.; Song, Y. F. et al. All-optical phosphorene phase modulator with enhanced stability under ambient conditions. *Laser Photonics Rev.* **2018**, *12*, 1800016.
[194] Ji, Q. Q.; Zhang, Y.; Zhang, Y. F.; Liu, Z. F. Chemical vapour deposition of group-VIB metal dichalcogenide monolayers: Engineered substrates from amorphous to single crystalline. *Chem. Soc. Rev.* **2015**, *44*, 2587–2602.
[195] Zhang, Y.; Zhang, L. Y.; Zhou, C. W. Review of chemical vapor deposition of graphene and related applications. *Acc. Chem. Res.* **2013**, *46*, 2329–2339.
[196] Lee, Y. H.; Zhang, X. Q.; Zhang, W. J.; Chang, M. T.; Lin, C. T.; Chang, K. D.; Yu, Y. C.; Wang, J. T. W.; Chang, C. S.; Li, L. J. et al. Synthesis of large-area MoS_2 atomic layers with chemical vapor deposition. *Adv. Mater.* **2012**, *24*, 2320–2325.
[197] Bae, S.; Kim, H.; Lee, Y.; Xu, X. F.; Park, J. S.; Zheng, Y.; Balakrishnan, J.; Lei, T.; Ri, K. H.; Song, Y. I. et al. Roll-to-roll production of 30-inch graphene films for transparent electrodes. *Nat. Nanotechnol.* **2010**, *5*, 574–578.
[198] Reina, A.; Jia, X. T.; Ho, J.; Nezich, D.; Son, H.; Bulovic, V.; Dresselhaus, M. S.; Kong, J. Large area, few-layer graphene films on arbitrary substrates by chemical vapor deposition. *Nano Lett.* **2009**, *9*, 30–35.
[199] Yoo, D.; Kim, M.; Jeong, S.; Han, J.; Cheon, J. Chemical synthetic strategy for single-layer transition-metal chalcogenides. *J. Am. Chem. Soc.* **2014**, *136*, 14670–14673.
[200] Mahler, B.; Hoepfner, V.; Liao, K.; Ozin, G. A. Colloidal synthesis of 1T-WS_2 and 2H-WS_2 nanosheets: Applications for photocatalytic hydrogen evolution. *J. Am. Chem. Soc.* **2014**, *136*, 14121–14127.
[201] Choucair, M.; Thordarson, P.; Stride, J. A. Gram-scale production of graphene based on solvothermal synthesis and sonication. *Nat. Nanotechnol.* **2009**, *4*, 30–33.
[202] Ren, X. H.; Zhou, J.; Qi, X.; Liu, Y. D.; Huang, Z. Y.; Li, Z. J.; Ge, Y. Q.; Dhanabalan, S. C.; Ponraj, J. S.; Wang, S. Y. et al. Few-layer black phosphorus nanosheets as electrocatalysts for highly efficient oxygen evolution reaction. *Adv. Energy Mater.* **2017**, *7*, 1700396.
[203] Xie, Z. J.; Xing, C. Y.; Huang, W. C.; Fan, T. J.; Li, Z. J.; Zhao, J. L.; Xiang, Y. J.; Guo, Z. N.; Li, J. Q.; Yang, Z. G. et al. Ultrathin 2D nonlayered tellurium nanosheets: Facile liquid-phase exfoliation, characterization, and photoresponse with high performance and enhanced stability. *Adv. Funct. Mater.* **2018**, *28*, 1705833.
[204] Li, Z. J.; Qiao, H.; Guo, Z. N.; Ren, X. H.; Huang, Z. Y.; Qi, X.; Dhanabalan, S. C.; Ponraj, J. S.; Zhang, D.; Li, J. Q. et al. High-performance photo-electrochemical photodetector based on liquid-exfoliated few-layered InSe nanosheets with enhanced stability. *Adv. Funct. Mater.* **2018**, *28*, 1705237.
[205] Backes, C.; Higgins, T. M.; Kelly, A.; Boland, C.; Harvey, A.; Hanlon, D.; Coleman, J. N. Guidelines for exfoliation, characterization and processing of layered materials produced by liquid exfoliation. *Chem. Mater.* **2017**, *29*, 243–255.
[206] Nicolosi, V.; Chhowalla, M.; Kanatzidis, M. G.; Strano, M. S.;

Coleman, J. N. Liquid exfoliation of layered materials. *Science* **2013**, *340*, 1226419.
[207] Tan, C. L.; Cao, X. H.; Wu, X. J.; He, Q. Y.; Yang, J.; Zhang, X.; Chen, J. Z.; Zhao, W.; Han, S. K.; Nam, G. H. et al. Recent advances in ultrathin two-dimensional nanomaterials. *Chem. Rev.* **2017**, *117*, 6225–6331.
[208] Tao, W.; Zhu, X. B.; Yu, X. H.; Zeng, X. W.; Xiao, Q. L.; Zhang, X. D.; Ji, X. Y.; Wang, X. S.; Shi, J. J.; Zhang, H. et al. Black phosphorus nanosheets as a robust delivery platform for cancer theranostics. *Adv. Mater.* **2017**, *29*, 1603276.
[209] Wang, S.; Weng, J.; Fu, X.; Lin, J.; Fan, W. P.; Lu, N.; Qu, J. L.; Chen, S. P.; Wang, T. F.; Huang, P. Black phosphorus nanosheets for mild hyperthermia-enhanced chemotherapy and chemo-photothermal combination therapy. *Nanotheranostics* **2017**, *1*, 208–216.
[210] Zhang, L. M.; Xia, J. G.; Zhao, Q. H.; Liu, L. W.; Zhang, Z. J. Functional graphene oxide as a nanocarrier for controlled loading and targeted delivery of mixed anticancer drugs. *Small* **2010**, *6*, 537–544.
[211] Sun, X. M.; Liu, Z.; Welsher, K.; Robinson, J. T.; Goodwin, A.; Zaric, S.; Dai, H. J. Nano-graphene oxide for cellular imaging and drug delivery. *Nano Res.* **2008**, *1*, 203–212.
[212] Naguib, M.; Kurtoglu, M.; Presser, V.; Lu, J.; Niu, J. J.; Heon, M.; Hultman, L.; Gogotsi, Y.; Barsoum, M. W. Two-dimensional nanocrystals produced by exfoliation of Ti_3AlC_2. *Adv. Mater.* **2011**, *23*, 4248–4253.
[213] Ghidiu, M.; Lukatskaya, M. R.; Zhao, M. Q.; Gogotsi, Y.; Barsoum, M. W. Conductive two-dimensional titanium carbide "clay" with high volumetric capacitance. *Nature* **2014**, *516*, 78–81.
[214] Lin, H.; Wang, X. G.; Yu, L. D.; Chen, Y.; Shi, J. L. Two-dimensional ultrathin MXene ceramic nanosheets for photothermal conversion. *Nano Lett.* **2017**, *17*, 384–391.
[215] Ji, X. Y.; Kong, N.; Wang, J. Q.; Li, W. L.; Xiao, Y. L.; Gan, S. T.; Zhang, Y.; Li, Y. J.; Song, X. R.; Xiong, Q. Q. et al. A novel top-down synthesis of ultrathin 2D boron nanosheets for multimodal imaging-guided cancer therapy. *Adv. Mater.* **2018**, *30*, 1803031.
[216] Cheng, Y.; Chang, Y.; Feng, Y. L.; Jian, H.; Tang, Z. H.; Zhang, H. Y. Deep-level defect enhanced photothermal performance of bismuth sulfide-gold heterojunction nanorods for photothermal therapy of cancer guided by computed tomography imaging. *Angew. Chem., Int. Ed.* **2018**, *57*, 246–251.
[217] Backes, C.; Szydłowska, B. M.; Harvey, A.; Yuan, S. J.; Vega-Mayoral, V.; Davies, B. R.; Zhao, P. L.; Hanlon, D.; Santos, E. J. G.; Katsnelson, M. I. et al. Production of highly monolayer enriched dispersions of liquid-exfoliated nanosheets by liquid cascade centrifugation. *ACS Nano* **2016**, *10*, 1589–1601.
[218] Liu, J.; Jiang, X. T.; Zhang, R. Y.; Zhang, Y.; Wu, L. M.; Lu, W.; Li, J. Q.; Li, Y. C.; Zhang, H. MXene-enabled electrochemical microfluidic biosensor: Applications toward multicomponent continuous monitoring in whole blood. *Adv. Funct. Mater.* **2019**, *29*, 1807326.
[219] He, J. S.; Tao, L. L.; Zhang, H.; Zhou, B.; Li, J. B. Emerging 2D materials beyond graphene for ultrashort pulse generation in fiber lasers. *Nanoscale* **2019**, *11*, 2577–2593.
[220] Tao, W.; Kong, N.; Ji, X. Y.; Zhang, Y. P.; Sharma, A.; Ouyang, J.; Qi, B. W.; Wang, J. Q.; Xie, N.; Kang, C. et al. Emerging two-dimensional monoelemental materials (Xenes) for biomedical applications. *Chem. Soc. Rev.* **2019**, *48*, 2891–2912.
[221] Ghorbanzadeh, R.; Assadian, H.; Chiniforush, N.; Parker, S.; Pourakbari, B.; Ehsani, B.; Alikhani, M. Y.; Bahador, A. Modulation of virulence in Enterococcus faecalis cells surviving antimicrobial photodynamic inactivation with reduced graphene oxide-curcumin: An *ex vivo* biofilm model. *Photodiagnsis Photodyn. Ther.* **2020**, *29*, 101643.
[222] Zhou, Y.; Zhang, M. X.; Guo, Z. N.; Miao, L. L.; Han, S. T.; Wang, Z. Y.; Zhang, X. W.; Zhang, H.; Peng, Z. C. Recent advances in black phosphorus-based photonics, electronics, sensors and energy devices. *Mater. Horiz.* **2017**, *4*, 997–1019.
[223] Song, Y. F.; Chen, S.; Zhang, Q.; Li, L.; Zhao, L. M.; Zhang, H.; Tang, D. Y. Vector soliton fiber laser passively mode locked by few layer black phosphorus-based optical saturable absorber. *Opt. Express* **2016**, *24*, 25933–25942.
[224] Du J; Zhang, M.; Guo, Z.; Chen, J.; Zhu, X.; Hu, G.; Peng, P.; Zheng, Z.; Zhang, H. Phosphorene quantum dot saturable absorbers for ultrafast fiber lasers. *Sci. Rep.* **2017**, *7*, 42357.
[225] Liang, X.; Ye, X. Y.; Wang, C.; Xing, C. Y.; Miao, Q. W.; Xie, Z. J.; Chen, X. L.; Zhang, X. D.; Zhang, H.; Mei, L. Photothermal cancer immunotherapy by erythrocyte membrane-coated black phosphorus formulation. *J. Controlled Release* **2019**, *296*, 150–161.
[226] Chen, W. S.; Ouyang, J.; Liu, H.; Chen, M.; Zeng, K.; Sheng, J. P.; Liu, Z. J.; Han, Y. J.; Wang, L. Q.; Li, J. et al. Black phosphorus nanosheet-based drug delivery system for synergistic photodynamic/photothermal/chemotherapy of cancer. *Adv. Mater.* **2017**, *29*, 1603864.
[227] Li, Y.; Liu, Z. M.; Hou, Y. Q.; Yang, G. C.; Fei, X. X.; Zhao, H. N.; Guo, Y. X.; Su, C. K.; Wang, Z.; Zhong, H. Q. et al. Multifunctional nanoplatform based on black phosphorus quantum dots for bioimaging and photodynamic/photothermal synergistic cancer therapy. *ACS Appl. Mater. Interfaces* **2017**, *9*, 25098–25106.
[228] Yang, X. Y.; Wang, D. Y.; Zhu, J. W.; Xue, L.; Ou, C. J.; Wang, W. J.; Lu, M.; Song, X. J.; Dong, X. C. Functional black phosphorus nanosheets for mitochondria-targeting photothermal/photodynamic synergistic cancer therapy. *Chem. Sci.* **2019**, *10*, 3779–3785.
[229] Chimene, D.; Alge, D. L.; Gaharwar, A. K. Two-dimensional nanomaterials for biomedical applications: Emerging trends and future prospects. *Adv. Mater.* **2015**, *27*, 7261–7284.
[230] Dong, H. F.; Tang, S. S.; Hao, Y. S.; Yu, H. Z.; Dai, W. H.; Zhao, G. F.; Cao, Y.; Lu, H. T.; Zhang, X. J.; Ju, H. X. Fluorescent MoS_2 quantum dots: Ultrasonic preparation, up-conversion and down-conversion bioimaging, and photodynamic therapy. *ACS Appl. Mater. Interfaces* **2016**, *8*, 3107–3114.
[231] Yong, Y.; Zhou, L. J.; Gu, Z. J.; Yan, L.; Tian, G.; Zheng, X. P.; Liu, X. D.; Zhang, X.; Shi, J. X.; Cong, W. S. et al. WS_2 nanosheet as a new photosensitizer carrier for combined photodynamic and photothermal therapy of cancer cells. *Nanoscale* **2014**, *6*, 10394–10403.
[232] Lin, L. S.; Cong, Z. X.; Li, J.; Ke, K. M.; Guo, S. S.; Yang, H. H.; Chen, G. N. Graphitic-phase C_3N_4 nanosheets as efficient photosensitizers and pH-responsive drug nanocarriers for cancer imaging and therapy. *J. Mater. Chem. B* **2014**, *2*, 1031–1037.
[233] Ju, E. G.; Dong, K.; Chen, Z. W.; Liu, Z.; Liu, C. Q.; Huang, Y. Y.; Wang, Z. Z.; Pu, F.; Ren, J. S.; Qu, X. G. Copper(II)-graphitic carbon nitride triggered synergy: Improved ROS generation and reduced glutathione levels for enhanced photodynamic therapy. *Angew. Chem., Int. Ed.* **2016**, *55*, 11467–11471.
[234] Chen, R.; Zhang, J. F.; Wang, Y.; Chen, X. F.; Zapien, J. A.; Lee, C. S. Graphitic carbon nitride nanosheet@metal-organic framework core-shell nanoparticles for photo-chemo combination therapy. *Nanoscale* **2015**, *7*, 17299–17305.
[235] Jiang, X. T.; Zhang, L. J.; Liu, S. X.; Zhang, Y. Y.; He, Z. L.; Li, W. J.; Zhang, F.; Shi, Y. H.; Lü, W.; Li, Y. et al. Ultrathin metal-organic framework: An emerging broadband nonlinear optical material for ultrafast photonics. *Adv. Opt. Mater.* **2018**, *6*, 1800561.
[236] Li, Y. F.; Di, Z. H.; Gao, J. H.; Cheng, P.; Di, C. Z.; Zhang, G.; Liu, B.; Shi, X. H.; Sun, L. D.; Li, L. L. et al. Heterodimers made of upconversion nanoparticles and metal-organic frameworks. *J. Am. Chem. Soc.* **2017**, *139*, 13804–13810.
[237] Zhu, W. J.; Yang, Y.; Jin, Q. T.; Chao, Y.; Tian, L. L.; Liu, J. J.; Dong, Z. L.; Liu, Z. Two-dimensional metal-organic-framework as a unique theranostic nano-platform for nuclear imaging and chemo-photodynamic cancer therapy. *Nano Res.* **2019**, *12*, 1307–1312.
[238] Lan, G. X.; Ni, K. Y.; Xu, R. Y.; Lu, K. D.; Lin, Z. K.; Chan, C.; Lin, W. B. Nanoscale metal-organic layers for deeply penetrating X-ray-induced photodynamic therapy. *Angew. Chem., Int. Ed.* **2017**, *56*, 12102–12106.
[239] Jiang, Z. W.; Zou, Y. C.; Zhao, T. T.; Zhen, S. J.; Li, Y. F.; Huang, C. Z. Controllable synthesis of porphyrin-based 2D lanthanide metal–organic frameworks with thickness- and metal-node-dependent photocatalytic performance. *Angew. Chem., Int. Ed.* **2020**, *59*, 3300–3306.
[240] Liu, J.; Jiang, X. T.; Zhang, R. Y.; Zhang, Y.; Wu, L. M.; Lu, W.; Li, J. Q.; Li, Y. C.; Zhang, H. MXene-enabled electrochemical microfluidic biosensor: Applications toward multicomponent continuous monitoring in whole blood. *Adv. Funct. Mater.* **2019**,

29, 1807326.

[241] Liu, G. Y.; Zou, J. H.; Tang, Q. Y.; Yang, X. Y.; Zhang, Y. W.; Zhang, Q.; Huang, W.; Chen, P.; Shao, J. J.; Dong, X. C. Surface modified Ti_3C_2 MXene nanosheets for tumor targeting photothermal/photodynamic/chemo synergistic therapy. *ACS Appl. Mater. Interfaces* **2017**, *9*, 40077–40086.

[242] Hu, T. Y.; He, J.; Zhang, S. M.; Mei, X.; Zhang, W. K.; Liang, R. Z.; Wei, M.; Evans, D. G.; Duan, X. An ultrathin photosensitizer for simultaneous fluorescence imaging and photodynamic therapy. *Chem. Commun.* **2018**, *54*, 5760–5763.

[243] Guan, S. Y.; Yang, D.; Weng, Y. Z. W.; Lu, H.; Meng, X. M.; Qu, X. Z.; Zhou, S. Y. Excitation-dependent theranostic nanosheet for cancer treatment. *Adv. Healthc. Mater.* **2018**, *7*, 1701123.

[244] Gao, R.; Mei, X.; Yan, D. P.; Liang, R. Z.; Wei, M. Nano-photosensitizer based on layered double hydroxide and isophthalic acid for singlet oxygenation and photodynamic therapy. *Nat. Commun.* **2018**, *9*, 2798.

[245] Pan, C.; Ou, M. T.; Cheng, Q. Z.; Zhou, Y.; Yu, Y. K.; Li, Z. M.; Zhang, F.; Xia, D. H.; Mei, L.; Ji, X. Y. Z-Scheme heterojunction functionalized pyrite nanosheets for modulating tumor microenvironment and strengthening photo/chemodynamic therapeutic effects. *Adv. Funct. Mater.* **2020**, *30*, 1906466.

[246] Song, C. Q.; Yang, C. Y.; Wang, F.; Ding, D. D.; Gao, Y.; Guo, W.; Yan, M.; Liu, S. Q.; Guo, C. S. MoS_2-based multipurpose theranostic nanoplatform: Realizing dual-imaging-guided combination phototherapy to eliminate solid tumor via a liquefaction necrosis process. *J. Mater. Chem. B* **2017**, *5*, 9015–9024.

[247] Zheng, D. W.; Li, B.; Li, C. X.; Fan, J. X.; Lei, Q.; Li, C.; Xu, Z. S.; Zhang, X. Z. Carbon-dot-decorated carbon nitride nanoparticles for enhanced photodynamic therapy against hypoxic tumor via water splitting. *ACS Nano* **2016**, *10*, 8715–8722.

[248] Yang, L. F.; Wang, J. P.; Yang, S.; Lu, Q. L.; Li, P. S.; Li, N. Rod-shape MSN@MoS_2 nanoplatform for FL/MSOT/CT imaging-guided photothermal and photodynamic therapy. *Theranostics* **2019**, *9*, 3992–4005.

[249] Jia, L.; Ding, L.; Tian, J. W.; Bao, L.; Hu, Y. P.; Ju, H. X.; Yu, J. S. Aptamer loaded MoS_2 nanoplates as nanoprobes for detection of intracellular ATP and controllable photodynamic therapy. *Nanoscale* **2015**, *7*, 15953–15961.

[250] Huang, P.; Xu, C.; Lin, J.; Wang, C.; Wang, X. S.; Zhang, C. L.; Zhou, X. J.; Guo, S. W.; Cui, D. X. Folic acid-conjugated graphene oxide loaded with photosensitizers for targeting photodynamic therapy. *Theranostics* **2011**, *1*, 240–250.

[251] Wang, R. H.; Li, X. H.; Wang, Z. X.; Zhang, H. Electrochemical analysis graphite/electrolyte interface in lithium-ion batteries: P-Toluenesulfonyl isocyanate as electrolyte additive. *Nano Energy* **2017**, *34*, 131–140.

[262] Li, P. F.; Chen, Y.; Yang, T. S.; Wang, Z. Y.; Lin, H.; Xu, Y. H.; Li, L.; Mu, H. R.; Shivananju, B. N.; Zhang, Y. P. et al. Two-dimensional $CH_3NH_3PbI_3$ perovskite nanosheets for ultrafast pulsed fiber lasers. *ACS Appl. Mater. Interfaces* **2017**, *9*, 12759–12765.

[253] Qi, X.; Zhang, Y. P.; Ou, Q. D.; Ha, S. T.; Qiu, C. W.; Zhang, H.; Cheng, Y. B.; Xiong, Q. H.; Bao, Q. L. Photonics and optoelectronics of 2D metal-halide perovskites. *Small* **2018**, e1800682.

[254] Zhang, Y. P.; Lim, C. K.; Dai, Z. G.; Yu, G. N.; Haus, J. W.; Zhang, H.; Prasad, P. N. Photonics and optoelectronics using nano-structured hybrid perovskite media and their optical cavities. *Phys. Rep.* **2019**, *795*, 1–51.

[255] Xing, C. Y.; Jing, G. H.; Liang, X.; Qiu, M.; Li, Z. J.; Cao, R.; Li, X. J.; Fan, D. Y.; Zhang, H. Graphene oxide/black phosphorus nanoflake aerogels with robust thermo-stability and significantly enhanced photothermal properties in air. *Nanoscale* **2017**, *9*, 8096–8101.

[256] Xie, Z. J.; Chen, S. Y.; Duo, Y. H.; Zhu, Y.; Fan, T. J.; Zou, Q. S.; Qu, M. M.; Lin, Z. T.; Zhao, J. L.; Li, Y. et al. Biocompatible two-dimensional titanium nanosheets for multimodal imaging-guided cancer theranostics. *ACS Appl. Mater. Interfaces* **2019**, *11*, 22129–22140.

[257] Chen, Y. J.; Wu, Y. K.; Sun, B. B.; Liu, S. J.; Liu, H. Y. Two-dimensional nanomaterials for cancer nanotheranostics. *Small* **2017**, *13*, 1603446.

[258] Chow, E. K. H.; Ho, D. Cancer nanomedicine: From drug delivery to imaging. *Sci. Transl. Med.* **2013**, *5*, 216rv4.

[259] Longmire, M.; Choyke, P. L.; Kobayashi, H. Clearance properties of nano-sized particles and molecules as imaging agents: Considerations and caveats. *Nanomedicine* **2008**, *3*, 703–717.

[260] Kapri, S.; Bhattacharyya, S. Molybdenum sulfide-reduced graphene oxide p-n heterojunction nanosheets with anchored oxygen generating manganese dioxide nanoparticles for enhanced photodynamic therapy. *Chem. Sci.* **2018**, *9*, 8982–8989.

[261] Ou, Q. D.; Zhang, Y. P.; Wang, Z. Y.; Yuwono, J. A.; Wang, R. B.; Dai, Z. G.; Li, W.; Zheng, C. X.; Xu, Z. Q.; Qi, X. et al. Strong depletion in hybrid perovskite p-n junctions induced by local electronic doping. *Adv. Mater.* **2018**, *30*, 1705792.

[262] Moole, H.; Tathireddy, H.; Dharmapuri, S.; Moole, V.; Boddireddy, R.; Yedama, P.; Dharmapuri, S.; Uppu, A.; Bondalapati, N.; Duvvuri, A. Success of photodynamic therapy in palliating patients with nonresectable cholangiocarcinoma: A systematic review and meta-analysis. *World J. Gastroenterol.* **2017**, *23*, 1278–1288.

[263] Cheon, Y. K.; Lee, T. Y.; Lee, S. M.; Yoon, J. Y.; Shim, C. S. Longterm outcome of photodynamic therapy compared with biliary stenting alone in patients with advanced hilar cholangiocarcinoma. *HPB* **2012**, *14*, 185–193.

[264] Gonzalez-Carmona, M. A.; Bolch, M.; Jansen, C.; Vogt, A.; Sampels, M.; Mohr, R. U.; van Beekum, K.; Mahn, R.; Praktiknjo, M.; Nattermann, J. et al. Combined photodynamic therapy with systemic chemotherapy for unresectable cholangiocarcinoma. *Aliment Pharmacol. Ther.* **2019**, *49*, 437–447.

[265] Kimura, M.; Miyajima, K.; Kojika, M.; Kono, T.; Kato, H. Photodynamic Therapy (PDT) with chemotherapy for advanced lung cancer with airway stenosis. *Int. J. Mol. Sci.* **2015**, *16*, 25466–25475.

[266] Autio, K. A.; Dreicer, R.; Anderson, J.; Garcia, J. A.; Alva, A.; Hart, L. L.; Milowsky, M. I.; Posadas, E. M.; Ryan, C. J.; Graf, R. P. et al. Safety and efficacy of BIND-014, a docetaxel nanoparticle targeting prostate-specific membrane antigen for patients with metastatic castration-resistant prostate cancer: A phase 2 clinical trial. *JAMA Oncol.* **2018**, *4*, 1344–1351.

[267] Lee, H.; Shields, A. F.; Siegel, B. A.; Miller, K. D.; Krop, I.; Ma, C. X.; LoRusso, P. M.; Munster, P. N.; Campbell, K.; Gaddy, D. F. et al. ^{64}Cu-MM-302 positron emission tomography quantifies variability of enhanced permeability and retention of nanoparticles in relation to treatment response in patients with metastatic breast cancer. *Clin. Cancer Res.* **2017**, *23*, 4190–4202.

[268] Wollina, U.; Gaber, B.; Koch, A. Photodynamic treatment with nanoemulsified 5-aminolevulinic acid and narrow band red light for field cancerization due to occupational exposure to ultraviolet light irradiation. *Georgian Med. News* **2018**, *274*, 138–143.